Department of Physics and Astronomy
University of Heidelberg

Hyperfine optical resonance fluorescence spectrum of titaniumlike ions

Bachelor Thesis in Physics
submitted by

Ioannis Stasinopoulos

born in Maroussi, Athens (Greece)

2011

This Bachelor Thesis has been carried out by Ioannis Stasinopoulos at the
Max Planck Institute for Nuclear Physics in Heidelberg
under the supervision of
Prof. Dr. Christoph H. Keitel
and
Dr. José R. Crespo López-Urrutia.

Abstract

In this thesis, the visible resonance fluorescence spectrum for heavy titaniumlike ions (e.g. $^{209}Bi^{61+}$) with nonvanishing nuclear spin is investigated theoretically. The research of such highly charged ions is motivated by potential applications related to the analysis of visible emission or absorption spectra obtained from measurements with electron beam ion traps (EBITs), tokamak and astronomical plasmas. Such studies may also assist future testing of the magnetic sector of quantum electrodynamics (QED) in strong fields and the determination of nuclear electromagnetic moments. We perform multiconfiguration Dirac-Fock calculations with additional QED corrections. Interactions between the electronic and nuclear multipole moments or an external magnetic field are treated within first-order perturbation theory, yielding the hyperfine or Zeeman energy splittings, respectively. The energy levels and magnetic dipole decay rates have been calculated for $^{209}Bi^{61+}$. A formula for the resonance fluorescence cross section has been derived within a relativistic transition operator formalism. The energy-dependent absorption cross section has been given and analyzed for a range of external magnetic field strengths, such as for 0, 1 and 8 T, and assuming different values for the Doppler broadening of the spectral lines. These theoretical spectra are intended to guide ongoing experimental activities. We have shown that the perturbative ansatz applies for the case of low magnetic fields in the vicinity of 1 T and needs to be improved for higher fields such as 8 T.

Zusammenfassung

In dieser Arbeit wird das sichtbare Resonanzfluoreszenzspektrum von schweren titanartigen Ionen (z.B. $^{209}Bi^{61+}$) mit nichtverschwindendem Kernspin theoretisch behandelt. Die Untersuchung von solchen hochgeladenen Ionen wird motiviert durch potentielle Anwendungen in der Analyse von sichtbaren Emissions- oder Absorptionsspektren aus Messungen in EBITs (Electron Beam Ion Traps), Tokamak- oder astronomischen Plasmas. Solche Untersuchungen könnten in Zukunft zu der Überprüfung der Quantenelektrodynamik (QED) in starken Feldern und zu der Bestimmung von kernmagnetischen Momenten beitragen. Eine Multikonfigurations-Dirac-Hartree-Fock Rechnung mit zusätzlichen QED Korrekturen wird durchgeführt. Die Wechselwirkungen zwischen den elektronischen und den nuklearen Multipolmomenten oder einem äußeren Magnetfeld werden in Störungstheorie erster Ordnung behandelt, was jeweils zu der Hyperfein- oder Zeeman Aufspaltung der Energien führt. Die Energieniveaus und magnetische-Dipol Zerfallsraten wurden für $^{209}Bi^{61+}$ ausgerechnet. Eine Formel für den Wirkungsquerschnitt der Resonanzfluoreszenz wurde in einem relativistischen Übergangsoperatorformalismus hergeleitet. Der energieabhängige Absorptionswirkungsquerschnitt wurde angegeben und für einen Bereich von Magnetfeldstärken, wie 0, 1 und 8 T, unter verschiedenen Werten der Dopplerverbreiterung analysiert. Diese theoretische Spektren sind als Leitfaden für aktuell ablaufende Experimente gedacht. Es wurde gezeigt, dass der störungstheoretische Ansatz im Falle von niedrigen äußeren Magnetfeldern in der Nähe von 1 T zutrifft und dass er bei höheren Magnetfeldstärken, wie 8 T, verbessert werden sollte.

Contents

Chapter 1

Introduction

1.1 Highly Charged Ions

The investigation of highly charged ions (HCIs) provides new insight into a broad range of physical phenomena.[1] These ions with massively reduced number of electrons, in comparison to their neutral counterparts, are abundant in outer space, especially in stars, such as our Sun, however, they are rare on Earth. The reason therefore lies in the large amount of energy needed to extract most bound electrons by ionizing the atoms. A very hot environment, such as a star can provide such energy and can thus lead to the creation of HCIs as part of a natural process, fusion. As opposed to that, on Earth technically challenging devices, like electron beam ion traps (EBITs), storage rings and tokamaks have been developed for their creation, storage and examination.

One source of interest in the analysis of HCIs lies in astrophysics, where they are responsible for the intensive part of the electromagnetic spectrum of stars. This happens because they are both heavy elements and highly charged at the same time, thereby radiating more intensively than lighter elements and neutral atoms. By examining their emission or absorption spectra, conclusions about their building mechanisms in galactic objects can be carried out.

Another motivation of the study of highly charged ions relates to basic research in quantum electrodynamics (QED), which ultimately describes the structure of atoms and their dynamics. To illustrate this, let us consider the following simple scaling law for one-electron ions relating the orbital radius R of an atomic electron to the Bohr radius a_0 and the nuclear charge Z:

$$R \propto \frac{a_0}{Z} \tag{1.1.1}$$

[1] Some information contained in this introduction is based on the articles [6, 15].

For a heavy system such as bismuth with Z=83, R falls below the Compton wavelength of the electron ($\lambda_C = \hbar m_e c \approx 2\,\mathrm{pm}$). Below this cutoff length quantum field theory takes over for the description of quantum mechanical systems, where the structure of vacuum and its influence by strong fields become significant. So far, QED is a successful field theory, since it has passed many reliability tests in weak electric and magnetic fields. However, open questions under strong field conditions persist, which motivate the testing of QED in strong electromagnetic fields with ever improving precision. In this concept HCIs offer ideal experimental conditions for obtaining strong static electric fields.

Moreover, testing the QED of bound systems, relativistic atomic structure theory, parity violation effects and nuclear contributions can be examined experimentally. One significant nuclear effect arises from the magnetic dipole and electric quadrupole moment of a nucleus with nonvanishing spin, which gives rise to the hyperfine splitting of spectral lines.

HCIs may not only be employed in basic research, but have also numerous applications. Microelectronics and nanotechnology, quantum computing, fusion energy technology, medicine and biotechnology are all fields to which HCIs contribute with their unique features.

1.2 Titaniumlike Ions

In this work the atomic structure of titaniumlike ions is calculated in a relativistic manner. Ti-like ions have a similar electronic configuration as the neutral titanium atom. They have 22 bound electrons, arranged in a [Ar]$3d^4$ configuration, which denotes a configuration identical to that of the noble gas argon with 4 additional electrons in the $3d$ subshell. The scaling of the fine structure splitting energies ($\propto$ emitted photon energies) is in general proportional to Z^4 due to relativistic effects and spin-orbit interaction [17], shifting thereby the visible-light spectrum rapidly into the x-ray regime with increasing Z. However, the $3d^4\ {}^5D_3 \leftrightarrow {}^5D_2$ magnetic dipole (M1) tranistion[2] in Ti-like ions is an exception to this rule, due to crossing of energy levels leading to an almost Z-independent variation of wavelength over a large portion of the isoelectronic sequence [4]. At the same time, a Z^3-scaling of the hyperfine interaction magnifies its effect to an observable level for high-Z elements. This is the case despite the fact that even though $3d$ electrons, which are generally weakly sensitive to nuclear effects, are involved in the transition. Thus, high-resolution spectroscopy can lead to the observation of hyperfine splitting in the optical regime.

[2]Notation: "${}^{2S+1}L_J$" : L, S, J are the many-electron orbital angular momentum, spin and total angular momentum quantum numbers, respectively.

Another particularity of HCIs lies in the coupling scheme of the orbital angular momentum and spin of the electrons. The spin-orbit interaction grows as Z^4 along the isoelectronic sequence. It is thus preferable to treat each electron individually, coupling first its spin and angular momenta $\vec{s}$ and $\vec{l}$ to $\vec{j}$ and then coupling the electronic $\vec{j}$-s *subsequently*, rather than coupling the total electron angular momentum $\vec{L}$ with the total electron spin $\vec{S}$ ($\vec{L}\vec{S}-$coupling). In this work the first coupling scheme has been used. This also implies that a fully relativistic treatment employing 4-component Dirac wavefunctions is highly desirable to accurately describe electrons bound in strong nuclear fields.

1.3 The Present Work

The aim of this thesis is to provide a theoretical prediction of the hyperfine-split optical absorption spectrum of heavy titaniumlike ions, which may be tested by an experiment planned to be conducted by the EBIT experimental group at the Max Planck Institute for Nuclear Physics in Heidelberg. The calculation of an electromagnetic spectrum for the so-called resonance fluorescence process is intended to assist the experimentalists in localizing and identifying the resonance lines characterized by hyperfine and Zeeman splittings, as far as these are expected to be seen, given the actual experimental resolution.

The theoretical work consists of the following steps:

1. the derivation of a formula for the total cross section of resonant photon scattering by applying a relativistic transition operator formalism,

2. the numerical MCDF (Multiconfiguration Dirac-Hartree-Fock) calculation of level energies, hyperfine and Zeeman splitting intervals and transition rates between atomic energy levels using the "General Relativistic Atomic Structure Program" (GRASP),

3. the generation of possible transitions due to the interaction with the electromagnetic field and, finally, the analysis of the calculated spectra.

Chapter 2

The Multiconfiguration Dirac-Fock Method

In this chapter the multiconfiguration Dirac-Fock (MCDF) procedure is explained, which is needed for obtaining an explicit representation of the wave functions of bound states of an N-electron atom. It is an extension of the Dirac-Hartree-Fock method (DF), which in turn generalizes the Hartree-Fock-Procedure according to the relativistic Dirac theory of electrons. The description follows Ref. [2].

2.1 The Dirac-Coulomb Hamiltonian for an N-Electron Atom

The Hamilton operator for an N-electron atom is given by

$$H_e^{DC} = \sum_{i=1}^{N} h_i + \sum_{i<j}^{N} \frac{e^2}{|\vec{r}_i - \vec{r}_j|}\,, \tag{2.1.1}$$

where

$$h_i = c\vec{\alpha}_i\vec{p}_i + (\beta_i - 1)m_e c^2 + V_{nuc}(r) \tag{2.1.2}$$

is the one-particle Dirac operator. The α_i and β_i are the 4×4 Dirac matrices and the subtraction of the unity matrix ensures that the one-particle energies are measured with respect to the rest energy $m_e c^2$. The form of $V_{nuc}(r)$ is described below.

In the usual, non-relativistic Hartree-Fock procedure, the atomic state with the lowest energy is found in a space of N-electron wave functions. This is achieved by variation of *test functions* in an iterative procedure. In the relativistic variant, i.e. the DF procedure, only the Hamiltonian and the wave functions (now four-component bispinors) differ. However, in our case, eigenstates of the Hamiltonian in the negative continuum are neglected, since the energy spectrum of the one-particle Dirac operators h_i is *not* bounded. The test functions are built from antisymmetrized product functions of one-particle wave functions, the Slater determinants. In MCDF theory, the eigenstates of the many-particle Hamilton operator (2.1.1) and therefore the final atomic states are constructed from *linear combinations of configuration state functions*, that is, of a combination of Slater determinants with different electron population and inner symmetry. This construction will be described in detail in Section 2.3 and 2.4.

2.2 Relativistic one-particle orbitals

A *Dirac orbital* or *Dirac one-particle wave function* $|n\kappa m\rangle$ is an eigenfunction of the total angular momentum operators $\vec{j}^2$, j_z, and of the relativistic parity operator $\mathcal{P}$:

$$\begin{aligned} \vec{j}^2|n\kappa m\rangle &= j(j+1)|n\kappa m\rangle, && (2.2.1)\\ j_z|n\kappa m\rangle &= m|n\kappa m\rangle, && (2.2.2)\\ \mathcal{P}|n\kappa m\rangle &= (-1)^l|n\kappa m\rangle. && (2.2.3) \end{aligned}$$

Here, l stands for the orbital angular momentum of the large component of the wave function and n stands for the principal quantum number. For the *Dirac angular momentum quantum number* κ holds:

$$\kappa = (-1)^{j+l+\frac{1}{2}}(j+\tfrac{1}{2}), \qquad l = j \pm \tfrac{1}{2} \qquad \Rightarrow \qquad j = |\kappa| - \tfrac{1}{2}\ . \tag{2.2.4}$$

An explicit representation of the one-particle wave function $|n\kappa m\rangle$ is the following:

$$\psi_{n\kappa m}(\vec{r}) \equiv \langle \vec{r}|n\kappa m\rangle = \frac{1}{r}\begin{pmatrix} P_{n\kappa}(r)\Omega^m_\kappa(\hat{r}) \\ iQ_{n\kappa}(r)\Omega^m_{-\kappa}(\hat{r}) \end{pmatrix}, \tag{2.2.5}$$

where $\hat{r}$ denotes the direction of $\vec{r}$, $P_{n\kappa}(r)$ and $Q_{n\kappa}(r)$ represent the *radial* wave functions of the large and small components of the Dirac bispinor, respectively, so that $\psi_{n\kappa m}(\vec{r})$ is a 4-component bispinor as demanded by the Dirac theory. They are chosen in such a way that the one-particle states

form an *orthonormal* set. This means that for two bound orbitals a and b the following integral relation holds:

$$\langle n_a\kappa_a m_a | n_b\kappa_b m_b\rangle = \int_0^\infty dr(P_{n_a\kappa_a}(r)P_{n_b\kappa_b}(r) + Q_{n_a\kappa_a}(r)Q_{n_b\kappa_b}(r)) = \delta_{ab} \ . \tag{2.2.6}$$

The spin- and angle-dependent part of the wave function is given by the *spherical spinor functions*:

$$\Omega^m_\kappa(\hat{r}) = \sum_{m_s} C(l\ \tfrac{1}{2}\ j; m-m_s, m_s\ m) Y_l^{m-m_s}(\hat{r})\chi_{m_s} \ , \tag{2.2.7}$$

where $C(\dots;\dots)$ is a Clebsch-Gordan coefficient [14], $Y_l^{m-m_s}(\hat{r})$ a spherical harmonic and χ_{m_s} a spinor basis function.

2.3 Configuration State Functions

In this section it is outlined how a wave function that describes an N-electron system (CSF) is built from one-particle orbital wave functions.

According to *Pauli's rule*, a CSF must be totally antisymmetric with respect to the coordinates of the electrons. The simplest way of obtaining such a wave function is using Slater determinants of the one-particle wave functions. Since the Hamilton operator (2.1.1) commutes with the operators of the *total* angular momentum of the N electrons, $\vec{J}^2$, and its z-component, J_z, it is handy to use eigenstates of these operators as the consisting elements of the CSFs. Therefore, the relativistic one-particle orbitals will be used. One CSF $|\gamma PJM\rangle$ is a *linear combination of Slater determinants of relativistic one-particle orbitals*, that are coupled to *the same* well-defined total angular momentum J. Clebsch-Gordan coefficients are used successively in the combination of the Slater determinants. A CSF is uniquely defined – with the exception of the phase – by the quantum numbers P of the parity, J of the angular momentum, the magnetic quantum number M, the configuration of the electrons and the way their angular momenta j_i are coupled to a total angular momentum J. The index γ describes the latter two.

2.3.1 Coupling of angular momenta in subshells

In the following the coupling scheme of the j_i of a given electron configuration will be presented on the example of the electronic states of helium, boron, carbon, and, finally, of titanium, which is of main interest along this work.

Starting with helium, we have two $1s$-electrons that possess $j = \frac{1}{2}$ each, since $l = 0$ and $s = \frac{1}{2}$. Following the coupling rule

$$|j_1 - j_2| \leq J \leq |j_1 + j_2| \tag{2.3.1}$$

incorporated in the Clebsch-Gordan coefficients and Pauli's exclusion principle, we get $[1s^2_{1/2}]_{0+}$ where "0+" denotes the total angular momentum of the *subshell* along with its parity. The latter is derived from the fact that one electron has the parity $\pi = (-1)^l$, with "l" being its orbit angular momentum quantum number and a many-electron system has $\pi = \prod_i \pi_i$.

Let us assume one has electrons that are distributed among more than one subshell, like, for example, in boron. In this case the coupling scheme will be as follows:

$$\Big[[1s^2]_0[2s^2]_0\ 2p_{1/2}\Big]_{1/2-} \qquad or \qquad \Big[[1s^2]_0[2s^2]_0\ 2p_{3/2}\Big]_{3/2-}$$

Now, $1/2-$ and $3/2-$ denote the total angular momentum and parity of the *total atomic electron shell*. They result from the successive coupling of the subshell angular momenta. The second possibility represents an excited state, since according to the Dirac theory, the states with same n but higher j possess higher energy.

The situation gets slightly more complicated with carbon. Here, the possible configurations are:

$$\Big[\big[1s^2\big]_0\big[2s^2\big]_0\big[2p^2_{1/2}\big]_0\Big]_{0+}$$

$$\Big[\big[1s^2\big]_0\big[2s^2\big]_0\big[2p_{1/2}\ 2p_{3/2}\big]_0\Big]_{\mathbf{1,2+}}$$

$$\Big[\big[1s^2\big]_0\big[2s^2\big]_0\big[2p^2_{3/2}\big]_0\Big]_{\mathbf{0,2+}}.$$

In the second one $|\frac{1}{2} - \frac{3}{2}| \leq J \leq |\frac{1}{2} + \frac{3}{2}|$ and in the third one $|\frac{3}{2} - \frac{3}{2}| \leq J \leq |\frac{3}{2} + \frac{3}{2}|$ so that we get two excited states in each case. In the latter the $J = 1, 3$ values are not permitted due to the Fermi exclusion principle [2].

When dealing with much larger electron occupations, one needs to refer to tables such as that in Ref. [2], p.429. There the possible values of the subshell angular momenta can be read out from the list and then easily be coupled to form the total angular momentum of the atomic electron shell. The electron

Table 2.1: Electron configuration in the peel shell $3d^4$ of the titaniumlike charge state and corresponding *atomic electron shell* total angular momenta J.

configuration		J
$[3d^4_{3/2}]_0$		0
$[3d^3_{3/2}]_{3/2}$	$3d^1_{5/2}$	1,2,3,4
$[3d^2_{3/2}]_2$	$[3d^2_{5/2}]_0$	2
	$[3d^2_{5/2}]_2$	0,1,3,4
	$[3d^2_{5/2}]_4$	2,3,4,5,6
$[3d^2_{3/2}]_0$	$[3d^2_{5/2}]_0$	0
	$[3d^2_{5/2}]_2$	2
	$[3d^2_{5/2}]_4$	4
$3d^1_{3/2}$	$[3d^3_{5/2}]_{3/2}$	0,1,2,3
	$[3d^3_{5/2}]_{5/2}$	1,2,3,4
	$[3d^3_{5/2}]_{9/2}$	3,4,5,6
	$3d^4_{5/2}$	0,2,4

configurations together with their values resulting from this procedure are summarized in Table 2.3.1 for the last and most complicated of our examples, titanium. This element has an electron configuration $\left[[\mathrm{Ar}]_0\ [3d^4]_J\right]_J$, where $[\mathrm{Ar}]_0$ denotes the configuration of argon, which has a total atomic electron shell angular momentum $J = 0$.

2.4 Atomic State Functions

We are now finally able to introduce the construction of the Atomic State Functions (ASFs), the eigenstates of the many-particle Hamilton operator (2.1.1) and therefore the final atomic states we are looking for. One ASF is nothing more than a finite linear combination of different CSFs with the *same* quantum numbers P, J and M[1]:

$$|\Gamma PJM\rangle = \sum_{r=1}^{n_c} c_{\Gamma r} |\gamma_r PJM\rangle \ . \tag{2.4.1}$$

Here, n_c is the number of the CSFs that are included in the calculation.

An example for an ASF for titanium could be:

$$\begin{aligned} \big|\Gamma, P=1, J=2, M\big\rangle \quad = \quad & c_1 \big|(3d^2_{3/2})_2 (3d^2_{5/2})_0 \ ; P=1, J=2, M\big\rangle + \\ & c_2 \big|(3d^3_{3/2})_{3/2} \ 3d^1_{5/2} \ ; P=1, J=2, M\big\rangle + \\ & c_3 \big|(3d^2_{3/2})_2 \ (3d^2_{5/2})_4 \ ; P=1, J=2, M\big\rangle + \\ & \dots \ , \end{aligned} \tag{2.4.2}$$

where the "..." represent the remaining configurations in Table 2.3.1. Notice that all the terms have the same total atomic electron shell angular momentum and that the order of the terms is chosen according to speculated dominance of the CSFs in the final atomic state: it is expected that c_1 will have a significantly greater value than the rest of the coefficients.

The set of mixing coefficients $c_{\Gamma r}$ may be combined in a column vector

$$\vec{c}_\Gamma = \begin{pmatrix} c_{\Gamma 1} \\ \vdots \\ c_{\Gamma n_c} \end{pmatrix} ,$$

which gives the representation of the atomic state $|\Gamma PJM\rangle$ with respect to the CSF *basis set* $\big\{|\gamma_r PJM\rangle\big\}_{r\in\{1,\dots,n_c\}}$. The ASFs are chosen to be orthonormal, so that

$$\langle \Gamma_i PJM | \Gamma_j PJM\rangle = \delta_{ij} \quad \text{for} \quad i,j \in \{1,\dots,n_a\} \tag{2.4.3}$$

$$\Leftrightarrow \sum_{r=1}^{n_c} c^*_{\Gamma r_i} c_{\Gamma r_j} \underbrace{\langle \gamma_r PJM | \gamma_r PJM\rangle}_{1} = \delta_{ij} \tag{2.4.4}$$

$$\Rightarrow \sum_{r=1}^{n_c} c^*_{\Gamma r_i} c_{\Gamma r_j} = (\vec{c}_{\Gamma i})^\dagger (\vec{c}_{\Gamma j}) = \delta_{ij} \, . \tag{2.4.5}$$

[1] Capital M refers to one of the $2J+1$ values of the magnetic quantum number of the *total atomic electron shell* angular momentum.

n_a with $n_a \leq n_c$ is the number of ASFs and the dagger denotes hermitian conjugation.
This requirement of orthonormalization implies that only after the action of an operator, such as, e.g. the dipole operator, the matrix element between two ASFs – that is, between two atomic states – cannot vanish. Otherwise the ASFs remain eigenstates of the many-particle Hamilton operator (2.1.1).

In summary it is left to note that expression (2.4.1) is nothing but an ansatz in the MCDF procedure, which expresses the idea that the final ASF will be a combination of many possible configurations, including excited states, where each one is more or less dominant according to the value of its mixing coefficient. It is these ASFs that will be used as the test functions mentioned in section 2.1.

2.5 The Self-Consistency Procedure

2.5.1 The eigenvalue problem

Having introduced the ASFs it will now be explained how the exact values of the mixing coefficients are obtained. The expectation value of the energy with respect to one ASF is

$$E_\Gamma^{DC} = \langle \Gamma PJM | H_e^{DC} | \Gamma PJM \rangle = \sum_{r,s=1}^{n_c} c_{\Gamma r}^* c_{\Gamma s} \langle \gamma_r PJM | H_e^{DC} | \gamma_s PJM \rangle \ . \tag{2.5.1}$$

We demand that, for a given set of CSFs, the expectation value E_Γ^{DC} is minimal with respect to variation of the coefficients. This leads after some calculation to the following eigenvalue problem:

$$\sum_{s=1}^{n_c} \Big(\langle \gamma_r PJM | H_e^{DC} | \gamma_s PJM \rangle - E_\Gamma^{DC} \delta_{rs} \Big) c_{s_\Gamma} = 0 \ . \tag{2.5.2}$$

If the Dirac orbital wave functions $|n\kappa m\rangle$ described in Section 2.2 are held constant, one refers to the *Configuration Interaction Procedure* (CI). Here only the c_{s_Γ}-s are varied. However, in the MCDF procedure the orbital wave functions are varied in addition. In this case there two options are available:

(a) **Optimized Level (OL) procedure**
The expectation value of the energy (2.5.1) is varied. This method is suitable for the calculation of the energy level and wave function

of a *single* atomic state. The rest of the configurations (orbitals) in (2.4.1) that are not optimized are called *correlation configurations*. It is expected that the quality of those atomic states is poorer than the optimized ones. It is precisely this issue that is treated in the second option below.

(b) **Average Level (AL) procedure**
A weighted mean value over all configurations

$$W^{DC} = \frac{\sum_{r=1}^{n_c}(2J_r+1)\langle\gamma_r PJM|H_e^{DC}|\gamma_r PJM\rangle}{\sum_{s=1}^{n_c}(2J_s+1)} \tag{2.5.3}$$

is minimized.

2.5.2 The Dirac-Fock equations

In general, the one-particle orbital wave functions are varied under their constraint of orthonormality (2.2.6) such that (2.5.1) or (2.5.3) become stationary. In both cases, this leads to the radial *Dirac-Fock equations* for a specific orbital with index a [2]:

$$\left(\frac{d}{dr}+\frac{\kappa_a}{r}\right)P_{n_a\kappa_a}(r)-\left(2c-\frac{\epsilon_a}{c}+\frac{Y_a(r)}{cr}\right)Q_{n_a\kappa_a}(r)=-\frac{\chi_a^P(r)}{r}\ , \tag{2.5.4}$$

$$\left(\frac{d}{dr}-\frac{\kappa_a}{r}\right)Q_{n_a\kappa_a}(r)+\left(-\frac{\epsilon_a}{c}+\frac{Y_a(r)}{cr}\right)P_{n_a\kappa_a}(r)=\frac{\chi_a^Q(r)}{r}\ . \tag{2.5.5}$$

The so-called *potential energy function* $Y_a(r)$ includes both the interaction with the nucleus, as well as the static potential that is produced by the charge distribution of the surrounding electrons via the electrostatic Coulomb interaction. A rather simple approximation to this function could be the Coulomb potential with an effective nuclear charge aimed to mimic the screening effect of the other electrons. However, a significantly better approximation is a potential based on the *Thomas-Fermi theory*, which provides an estimate of the radial variation of screening of the nuclear field.
Generally, in $Y_a(r)$ integrations over $Q_{n_a\kappa_a}(r)$ and $P_{n_a\kappa_a}(r)$ are included. Therefore, equations (2.5.4) and (2.5.5) are *integro-differential equations*, a fact which complicates their solution. Moreover ϵ_a is a *Lagrange multiplier* that ensures the boundary conditions for $Q_{n_a\kappa_a}(r)$ and $P_{n_a\kappa_a}(r)$ while c stands for the speed of light and $\chi_a^P(r)$ and $\chi_a^Q(r)$ are the *exchange potentials.* These arise from the exchangeability of the electrons, that is, from

the usage of Slater determinants. Consequently, when treating a one-particle problem like, e.g. one electron in interaction with an infinite-mass nucleus, these inhomogeneous terms vanish.
The simultaneous solution of the eigenvalue problem (2.5.2) for the mixing coefficients and of the coupled DF equations (2.5.4) & (2.5.5) for the radial wave functions is achieved through the *self-consistency procedure*. One begins with a set of given approximate functions. With these the Hamiltonian matrix is calculated and diagonalized and the mixing coefficients $c_{\Gamma r}$ are obtained. With those new coefficients and the original wave functions, the potentials $Y_a(r)$, $\chi_a^P(r)$ and $\chi_a^Q(r)$ are computed and, finally, the DF equations are numerically integrated. After this, one gets new wave functions with which the next iteration step begins. These steps are to be repeated until convergence is achieved, that is, until the variation of the mixing coefficients, the radial wave functions or energy eigenvalues remain under a pre-specified tolerance limit. A complete description of this procedure along with the exact expressions of $Y_a(r)$, $\chi_a^P(r)$ and $\chi_a^Q(r)$ can be found in [2].

2.6 The nucleus

2.6.1 Nuclear volume effect

The treatment of the nucleus as an extended object instead of a point charge is explained in the present subsection.

In atoms with high values of the atomic number, such as the case of this work, the energy eigenvalues of atomic states exhibit great dependence on the charge distribution of the nucleus. The following extended distributions exist:

(a) **Simple spherical ball distribution**

$$\rho_{nuc}(r) = \begin{cases} \rho_0, & \text{if} \quad r \leq r_{nuc}, \\ 0, & \text{otherwise} \ . \end{cases} \tag{2.6.1}$$

Here, r_{nuc} is the nuclear radius, which can be specified. GRASP[2] determines it according to the semi-empirical relation $r_{nuc} = (1.0793A^{1/3} + 0.73587)\,\text{fm}$, given in [11], if no other value is provided.

(b) **Fermi two-parameter distribution**

$$\rho_{nuc}(r) = \frac{\rho_0}{1 + e^{(r-c)/a}} \ . \tag{2.6.2}$$

[2]See more in appendix A.

The parameter c is the so-called *half-charge radius*, the value of r for which $\rho_{nuc}(r) = 0.5\,\rho_0$. Thus it provides a measure for the nuclear radius. Parameter a is connected to t through the relation $a = t\,4\ln 3$, where t is the *skin thickness* parameter, the interval across which $\rho_{nuc}(r)$ falls from $0.9\ \rho_0$ to $0.1\,\rho_0$.
The parameters c and a can be chosen freely in GRASP; alternatively, the root-mean-square radius can be calculated from the semi-empirical formula given above and t is set automatically to 2.30 fm.

In all cases, the nuclear potential is calculated from the charge distribution $\rho_{nuc}(r)$ using the integral relation

$$-rV_{nuc}(r) = 4\pi\left(\int_0^r \rho(s)s^2\,ds + r\int_r^\infty \rho(s)s\,ds\right). \tag{2.6.3}$$

The calculated $V_{nuc}(r)$ is the solution of the Poisson equation

$$\vec{\nabla}^2 V_{nuc}(r) = -4\pi\rho(r) \tag{2.6.4}$$

with the condition $V \to 0$ for $r \to \infty$. The parameter ρ_0 is determined in such a way that the integral over the whole charge distribution corresponds to the total electrical charge Z of the nucleus. The influence of $\rho_{nuc}(r)$ is most significant on the energy of the $1s_{1/2}$ state, since its wave function overlaps primarily with the nucleus.

2.6.2 Nuclear finite mass effects

Nuclear finite mass effects on the energy fall into two categories [12]:

(a) **Reduced mass correction**
Named also *normal mass shift,* it is accounted for by the replacement of the electron mass m_e by the reduced mass $\mu = \frac{m_e M}{m_e + M}$.

(b) **Corrections due to correlated motions of the electrons**
or specific mass shift.

2.7 QED Corrections to the MCDF Energies

In this section two types of additional interactions that have to be considered apart from the above-described MCDF procedure are presented: the *Breit interaction* and the *fluctuations of the electromagnetic* and *electron-positron field.*

2.7.1 The transverse electromagnetic interaction

In atoms with large atomic numbers, the *frequency-dependent Breit interaction* between electrons due to the exchange of a transverse photon has to be taken into account [2]. It represents a relativistic correction of the Coulomb interaction and describes *retardation effects* and the *magnetic interaction between two Dirac currents* in the Coulomb gauge.

The Breit interaction operator can be derived from the S-matrix element of the electron-electron scattering. It is given by

$$V^B(r_{12},\omega) = -\vec{\alpha}_1\vec{\alpha}_2\frac{\cos(\omega r_{12})}{r_{12}} + (\vec{\alpha}_1\vec{\nabla}_1)(\vec{\alpha}_2\vec{\nabla}_2)\frac{\cos(\omega r_{12})-1}{\omega^2 r_{12}}\ , \qquad (2.7.1)$$

with $r_{12} = |\vec{r}_1 - \vec{r}_2|$, ω being the frequency of the exchanged photon and $\vec{\alpha}$ being the Dirac α-matrix vector. In the context of MCDF theory, this *contributes the matrix elements*

$$H^B_{rs} = \langle\gamma_r PJM|V^B(\omega)|\gamma_s PJM\rangle, \qquad (2.7.2)$$

out of which the diagonal ones can simply be added to the MCDF energies. Alternatively, all the matrix elements (2.7.2) are added to the Dirac-Coulomb Hamiltonian matrix elements

$$H^{DC}_{rs} = \langle\gamma_r PJM|H^{DC}_e|\gamma_s PJM\rangle, \qquad (2.7.3)$$

where H^{DC}_e is the operator (2.1.1). The resulting matrix is then diagonalized.

2.7.2 Radiative Corrections

Two effects are included here:

(a) **electron self-energy (SE)**
This is the dominant radiative correction to the energy. It arises from the lowest-order modification of electronic interaction with the quantized ambient electromagnetic field of the nucleus and the other atomic electrons. The self-energy in a hydrogenlike system in lowest order of perturbation theory is given by [18]:

$$\Delta E^{\rm SE}_{n\kappa} = \frac{Z^4}{\pi c^3 n^3}F_{n\kappa}(Z)\,. \qquad (2.7.4)$$

The functions $F_{nk}(Z)$ vary slowly with respect to the nuclear charge Z and are tabulated for a range of states in the literature. In the GRASP

package, the self-energy of a one-particle state with quantum numbers $n_a\kappa_a$ is approximated by

$$\Delta E^{\mathrm{SE}}_{n_a\kappa_a} = \frac{(Z^{\mathrm{eff}})^4}{\pi c^3 n_a^3} \begin{cases} F_{n_a\kappa_a}(Z_a^{\mathrm{eff}}), & \text{for } 1s_{1/2},\ 2s_{1/2},\ 2p_{1/2} \text{ and } 2p_{3/2}, \\ F_{2\kappa_a}(Z_a^{\mathrm{eff}}), & \text{for } ns_{1/2},\ np_{1/2} \text{ and } np_{3/2} \text{ with } n > 2, \\ 0 & \text{otherwise}\,. \end{cases} \tag{2.7.5}$$

For the many-particle states, these one-electron contributions are summed. By the use of the effective atomic number Z_a^{eff}, electron screening effects are roughly included. The latter approximation is likely to be increasingly less realistic as the principle quantum number n increases.

(b) **vacuum polarization (VP)**
In order of importance the next effect is the vacuum polarization correction. To lowest order, this is the short-range modification of the nuclear field due to screening by virtual electron-positron pairs. Also here, the corrections to the orbitals $n_a\kappa_a$ are calculated by means of perturbation theory:

$$\Delta E^{\mathrm{U}}_{n_a\kappa_a} = \langle n_a\kappa_a | V^{\mathrm{U}} | n_a\kappa_a \rangle = \int_0^\infty dr\ V^{\mathrm{U}}(r) \left(P^2_{n_a\kappa_a}(r) + Q^2_{n_a\kappa_a}(r) \right), \tag{2.7.6}$$

with the *Uehling potential* $V^{\mathrm{U}}(r)$. In analogy to the self energy, contributions of individual electrons are additively superimposed.

Chapter 3

Resonant Photon Scattering Cross Section

In this chapter an expression for the total cross section of resonance fluorescence, i.e. the process consisting of atomic excitation by photon absorption and the subsequent de-excitation by photon emission, is derived. If, as in our case, the excited state cannot decay by other means, e.g. by autoionization, the resonance fluorescence cross section determines the total optical absorption cross section. We consider the case of a low-intensity exciting photon field, i.e. neglect multiphoton processes. We apply a transition operator formalism. As mentioned in Ref. [3], this method can be applied in a wide range of phenomena occurring in atomic and nuclear reactions and provides their intuitive understanding.

In order to obtain the required pseudo-spectrum, the total cross section of the resonance fluorescence process of the system has to be determined. The *differential cross section* is related to the T-matrix element by *Fermi's golden rule*[1]:

$$\frac{d\sigma_{i\to f}(E)}{d\Omega_{k_f}} = \frac{2\pi}{\hbar F_i}\left|\langle \Phi_f, \lambda_f \vec{k}_f | T(E) | \Phi_i, \lambda_i \vec{k}_i \rangle\right|^2 \rho_f. \tag{3.0.1}$$

Here F_i stands for the flux density of the incoming photons and ρ_f for the density of final photonic states. Φ_i, Φ_f refer to the initial and final bound electronic states of the system, respectively; λ and $\vec{k}$ to the polarization and wave vector of the photons. $d\Omega_{k_f}$ represents the solid angle element for the direction of the emitted photon with wave number k_f. T refers to the *transition operator*, for which en expression will be derived in Section 3.3. The

[1] see [17] p.807, 836

basic ideas of the calculations are extracted from the theoretical formalism of Haan and Jacobs [8].

3.1 Total Hamiltonian of the System

First of all, the relativistic Hamilton operator that describes our system composed of an atom or atomic ion of n_e electrons and the photon continuum is given by

$$H = H_e^{DC} + H_r + H_{er}\,, \tag{3.1.1}$$

where the Coulomb-Dirac Hamiltonian is given as

$$H_e^{DC} = \sum_{i=1}^{n_e} h_i + \sum_{i<j}^{n_e} \frac{e^2}{|\vec{r}_i - \vec{r}_j|} + \sum_{i=1}^{n_e} H_{hfs}(\vec{r}_i) - \vec{\mu_F}\vec{B}\,. \tag{3.1.2}$$

h_i is the one-particle Dirac Hamilton operator:

$$h_i = c\vec{\alpha}_i\vec{p}_i + (\beta_i - 1)mc^2 + V_{nuc}(r)\,, \tag{3.1.3}$$

e is the electron charge[2], m is its mass, and H_{hfs} is the one-particle Hamilton operator for the hyperfine interaction [12]:

$$H_{hfs}(\vec{r}) = e\phi(\vec{r}) - ec\vec{\alpha}\cdot\vec{A}(\vec{r})\,, \tag{3.1.4}$$

with

$$\vec{A}(\vec{r}) = \frac{1}{c^2}\frac{\vec{\mu_I}\times\vec{r}}{r^3} \tag{3.1.5}$$

being the magnetic vector potential corresponding to the nuclear magnetic moment $\vec{\mu}_I$, at position $\vec{r}$ relative to the nucleus and

$$\phi(\vec{r}) = \sum_{i,j}\frac{x_i x_j}{2r^5}Q_{ij} \tag{3.1.6}$$

the scalar potential with the nuclear quadrupole moment tensor Q_{ij}. The last term in H_e^{DC} describes the Hamiltonian of the Zeeman interaction of the magnetic moment of the atom $\vec{\mu}_F$ with an external magnetic field $\vec{B}$. More about this term and H_{hfs} will be described in Section 4.2.

$$H_r = \sum_{\vec{k}}\sum_{\lambda=1}^{2}\hbar\omega_{\vec{k}}a^\dagger_{\vec{k}\lambda}a_{\vec{k}\lambda} \tag{3.1.7}$$

[2] e has here the unit Coulomb; it has been chosen $1/(4\pi\epsilon_0) \equiv 1$, for reasons that will later become clear to the reader.

is the Hamiltonian of the free radiation (electromagnetic) field given in second-quantized form with $a^{\dagger}_{\vec{k}\lambda}$, $a_{\vec{k}\lambda}$ describing the creation and annihilation operator for a photon of momentum $\vec{k}$ and polarization $\lambda \in \{1,2\}$, respectively. Note that the radiation field can be in general linearly as well as circularly polarized; we consider here real transverse photons. Finally,

$$H_{er} = \sum_{i=1}^{n_e} \sum_{\vec{k}} \sum_{\lambda=1}^{2} \sqrt{\frac{2\pi\hbar c^2}{V\omega_k}} \vec{\alpha_i} \left(\vec{\epsilon}_{\vec{k}\lambda} e^{i\vec{k}\vec{r_i}} a_{\vec{k}\lambda} + \vec{\epsilon}^{*}_{\vec{k}\lambda} e^{-i\vec{k}\vec{r_i}} a^{\dagger}_{\vec{k}\lambda} \right) \tag{3.1.8}$$

describes the interaction between the electrons and the radiation field.
As usual, c represents the speed of light in vacuum. V is the quantization volume for the photon modes. The vector of the 4×4 α-matrices is

$$\vec{\alpha}_i = \begin{pmatrix} \alpha^x \\ \alpha^y \\ \alpha^z \end{pmatrix}_i \quad \text{with} \quad \alpha^k = \begin{pmatrix} 0 & \sigma^k \\ \sigma^k & 0 \end{pmatrix} \tag{3.1.9}$$

and the σ^k are the 2×2 Pauli matrices. $\vec{p_i} = -i\hbar\vec{\nabla}_i = -i\hbar \begin{pmatrix} \partial/\partial x \\ \partial/\partial y \\ \partial/\partial z \end{pmatrix}_i$ is the momentum operator of the i^{th} particle. $\omega_{\vec{k}} = ck = c|\vec{k}|$ is the frequency of a photon of the radiation field in the mode $\vec{k}$, $\vec{\epsilon}_{\vec{k}\lambda}$, $\vec{\epsilon}^{*}_{\vec{k}\lambda}$ are the normalized polarization vectors in direction of propagation of the plane wave and $V_{nuc}(r)$ is the nuclear potential of the atom, given in Section 2.6.

3.2 Projection Operators

Before introducing the expressions of the projection operators that will help us calculate the transition matrix element in equation (3.0.1), one should clarify that the system makes a transition through the following two types of states: the initial state is composed of bound electrons of the ion and $n+1$ incoming photons $\{\lambda_i^m \vec{k}_i^m\}_{m=1}^{n+1}$ from the radiation field, whereas the final state contains bound electrons and n emitted photons $\{\lambda_f^m \vec{k}_f^m\}_{m=1}^{n}$. The operator that projects onto the subspace of states containing one active photon $\lambda\vec{k}$ (the other n photons that are always present will not be considered for now) and bound electrons is given by [20]:

$$R = \sum_{\xi} \sum_{\lambda\vec{k}} |\Phi_\xi, \lambda\vec{k}\rangle\langle\Phi_\xi, \lambda\vec{k}| \ , \tag{3.2.1}$$

where ξ is a collective index that summarizes all the relevant quantum numbers needed to specify the bound electronic state[3]. The states given above are product states of the eigenstates of H_e and H_r. The summation goes over a complete set of atomic and photonic states.

The system however goes through an intermediate, *discrete* state as well. The operator that projects on the subspace of discrete bound states of the atom, where the active photon has been absorbed is:

$$Q = \sum_d |\Phi_d, 0\rangle\langle\Phi_d, 0| \tag{3.2.2}$$

Here, again, d stands for all the quantum numbers of the discrete atomic state, and in the definition of the projection operator one sums over all such possible states. The 0 representing that there is not a single active photon in this state has been used only once and for clarity will be omitted in the rest of this chapter.
The eigenstates of the above subspaces fulfill the orthonormalization conditions

$$\langle\Phi_\xi, \lambda\vec{k}|\Phi'_\xi, \lambda'\vec{k}'\rangle = \delta_{\xi\xi'}\delta_{\lambda\lambda'}\delta_{\vec{k}\vec{k}'}\,, \tag{3.2.3}$$

$$\langle\Phi_d|\Phi'_d\rangle = \delta_{dd'}\ . \tag{3.2.4}$$

As projection operators, R and Q respect the following orthogonality conditions

$$\begin{aligned} R^2 &= R\,, \\ Q^2 &= Q\,, \end{aligned}$$

$$RQ = QR = 0\,. \tag{3.2.5}$$

Furthermore we assume that the *completeness relation*

$$R + Q = 1 \tag{3.2.6}$$

is fulfilled. Equation (3.2.6) expresses actually an approximation, since (i) we work in the one-photon continuum (only one photon can be absorbed or emitted at a time), (ii) we do not consider ionization of the atom by the radiation field nor (iii) *autoionization* is possible (we consider transitions between deeply-bound hyperfine-structure states).

[3]It is actually the product state $|\Phi_\xi\rangle \bigotimes |\lambda\vec{k}\rangle$ that is meant by $|\Phi_\xi, \lambda\vec{k}\rangle$.

Applying perturbation theory, we decompose the total Hamiltonian into an unperturbed part and a perturbation:

$$H = H_0 + V \tag{3.2.7}$$

H_0 is not explicitly time dependent and possesses the known discrete eigenstates $|\Phi_d\rangle$ with energy E_d:

$$H_0|\Phi_d\rangle = E_d|\Phi_d\rangle \tag{3.2.8}$$

as well as the eigenstates $|\Phi_f; \lambda\vec{k}\rangle$, which are *product states* of a photon and bound discrete atomic states[4]

$$H_0|\Phi_f, \lambda\vec{k}\rangle = \big(E_f + \hbar\omega\big)\big|\Phi_f, \lambda\vec{k}\big\rangle\,. \tag{3.2.9}$$

Additionally, H_0 commutes with the previously defined projection operators: $H_0R = RH_0$ and $H_0Q = QH_0$.

Now considering the completeness relation (3.2.6), one can rewrite the Hamiltonian:

$$H = (R+Q)H(R+Q)\,, \tag{3.2.10}$$

and identify the H_0 and V as

$$H_0 = RHR + QHQ\,, \tag{3.2.11}$$
$$V = QHR + RHQ\,. \tag{3.2.12}$$

Here the discrete excited intermediate states are eigenstates of QHQ and RHR describes the Hamiltonian with the photonic continuum.

The interaction V is also assumed not to be explicitly time-dependent and its diagonal projections are equal to zero

$$RVR = 0\,, \quad QVQ = 0\,. \tag{3.2.13}$$

The operator V describes transitions between different subspaces, thus summing all the possible interactions. It is the one that couples the discrete states to the photon continuum (radiative excitation and decay). QHR describes therefore the excitation by photon absorption and RHQ the radiative decay.

[4]Compare with [17], p. 983, 984.

3.3 The Transition Operator T

We will now determine the transition operator T corresponding to our process of interest by a perturbative expansion. T depends on the total energy of the initial state E. It is given by[5]

$$T(z) = V + VG(z)V, \tag{3.3.1}$$

where

$$G(z) = [z - H]^{-1} \tag{3.3.2}$$

is the *Green operator* of the total Hamiltonian and z denotes the complex energy variable used to specify the appropriate scattering boundary conditions on the asymptotic continuum states. $G(z)$ can be formally calculated from the Lippmann-Schwinger equation

$$G(z) = G_0(z) + G_0(z)VG(z)\,, \tag{3.3.3}$$

or, equivalently,

$$(z - H_0)G(z) = 1 + VG(z)\,, \tag{3.3.4}$$

with $G_0(z) = [z - H_0]^{-1}$ being the Green operator of the unperturbed Hamiltonian. Using the closure relation $R + Q = 1$ one can express $T(z)$ as

$$\begin{aligned} T(z) &= V + V(R+Q)G(z)(R+Q)V \\ &= V + VRG(z)RV + VRG(z)QV + VQG(z)RV + VQG(z)QV. \end{aligned} \tag{3.3.5}$$

After defining the *continuum propagator*

$$\Phi(z) = R[R(z - H_0 - V)R]^{-1} \tag{3.3.6}$$

and taking into account that R commutes with H_0, the following useful relations can be obtained from multiplication of (3.3.4) with R and Q from the left/right

$$RG(z)R = R\Phi(z)R\big[1 + VQG(z)R\big]\,, \tag{3.3.7}$$

$$RG(z)Q = \big[R\Phi(z)R\big]V\big[QG(z)Q\big]\,, \tag{3.3.8}$$

$$QG(z)R = QG(z)Q\big[VR\Phi(z)R\big]\,. \tag{3.3.9}$$

[5] See for example [22], chapter 8.

Defining the *Level-Shift-Operator* as

$$\Lambda(z) = V + VR\Phi(z)RV\,, \tag{3.3.10}$$

and inserting equations (3.3.7)-(3.3.9) into (3.3.5), the transition operator is reduced to

$$T(z) = \Lambda(z) + \Lambda(z)QG(z)Q\Lambda(z). \tag{3.3.11}$$

The first term, $\Lambda(z)$, describes scattering in the absence of the set of the Q states.

Now for calculating the matrix element $\langle\Phi_f|RT(E)R|\Phi_i\rangle$ in equation[6] (3.0.1) we have to find an expression for $RT(z)R$, which describes the evolution of our system from an initial photon continuum state into a final one. Using (3.3.11) we get

$$RT(z)R = R\Lambda(z)R + R\Lambda(z)QG(z)Q\Lambda(z)R\,. \tag{3.3.12}$$

We will now continue evaluating the terms

$$R\Lambda(z)Q = RVQ + RVR\Phi(z)RVQ = RVQ = RH_{er}Q\,. \tag{3.3.13}$$

Since H_{er} is the only part of the Hamiltonian (3.1.1) that accounts for the transition from the discrete to the one-photon states, it is $V \equiv H_{er}$. In analogy:

$$Q\Lambda(z)R = QVR + QVR\Phi(z)RVR = QVR = QH_{er}R \tag{3.3.14}$$

With (3.3.13) and (3.3.14), (3.3.12) becomes

$$RT(z)R = R\Lambda(z)R + RH_{er}QG(z)QH_{er}R\,. \tag{3.3.15}$$

We must now find an expression for $QG(z)Q$. For this, one can start from

$$\begin{aligned} QG(z)Q &= Q\big(Q[z - H_0 - \Lambda(z)]Q\big)^{-1} \\ &= Q(Q[z - H - VR\Phi(z)RV]Q\big)^{-1}. \end{aligned} \tag{3.3.16}$$

The equality in the first line comes from substitution of (3.3.8) into an equivalent form[7] of (3.3.4) and for the second merely the definition of $\Lambda(z)$ has been used. Then the so-called *isolated resonances approximation* is performed, in which the non-diagonal matrix elements

$$\big\langle\Phi_d\big|Q[z - H - VR\Phi(z)RV]Q\big|\Phi_{d'}\big\rangle\,, \quad d \neq d'\,,$$

[6] $R|\Phi_i\rangle = |\Phi_i\rangle = |\Phi_i, \lambda\vec{k}\rangle$; accordingly for $R|\Phi_f\rangle$. Also $Q|\Phi_d\rangle = |\Phi_d\rangle = |\Phi_d, 0\rangle$.

[7] See [8], p.82.

are neglected. Using the approximation[8]

$$R\Phi(z)R \approx R[R(z-H_0)R]^{-1} = RG_0^R R \ , \tag{3.3.17}$$

with the Green operator $G_0^R(z) = [R(z-H_0)R]^{-1}$, the diagonal elements of the operator $Q[z-H-VR\Phi(z)RV]Q$ can be expressed as follows[9]:

$$\begin{aligned} &\big\langle \Phi_d \big| Q[z-H-VR\Phi(z)RV]Q \big| \Phi_{d'} \big\rangle \\ &\approx (z-E_d) - \langle \Phi_d | QVRG_0^R(z)RVQ | \Phi_d \rangle \end{aligned} \tag{3.3.18}$$

The second term of the latter can be split into a real and an imaginary part[10]:

$$\langle \Phi_d | QVRG_0^R(z)RVQ | \Phi_d \rangle = \Delta E_d^R - \frac{i}{2}\Gamma_d^R \, , \tag{3.3.19}$$

where ΔE_d^R describes self-energy and transverse-photon exchange corrections to the energy E_d for the intermediate state d [22]. The latter correction can be identified as the *Breit interaction* [16]. In the imaginary part, Γ_d^R stands for the *radiative width* of the state.

Employing equation (3.3.16), this brings us to the result:

$$QG(z)Q = \sum_d \frac{|Q\Phi_d\rangle\langle\Phi_d|}{z - E_d - \Delta E_d^R + \frac{i}{2}\Gamma_d^R} \ , \tag{3.3.20}$$

since $\sum_d |Q\Phi_d\rangle\langle\Phi_d| = Q$.

Finally, by inserting (3.3.20) into our main relation (3.3.15), the desired matrix element $\langle \Phi_f | RT(E)R | \Phi_i \rangle$, under the approximations discussed above, has the final form

$$\langle \Phi_f | RT(E)R | \Phi_i \rangle = \sum_d \frac{\langle \Phi_f | RH_{er}Q | \Phi_d \rangle \langle \Phi_d | QH_{er}R | \Phi_i \rangle}{z - E_d - \Delta E_d^R + \frac{i}{2}\Gamma_d^R}. \tag{3.3.21}$$

The term $R\Lambda(z)R$ in (3.3.12) describes the case, where the atom does not interact at all with the radiation field, which is not of interest to us; therefore it has been neglected. In the following, we will omit for clarity the energy correction ΔE_d^R, i.e. we assume that it is included in the level energy E_d.

We note that a similar calculation that introduced the complex energy shift (3.3.19) to the energy of level d may be done to yield the same correction to the energies of the initial and final ionic levels. These corrections are real, since those states are assumed to be stable, i.e. their radiative widths are (practically) zero.

[8] See appendix B.1.
[9] See appendix B.2.
[10] See [17], p.994-1001.

3.4 The Total Cross Section for Dipole Transition

Inserting (3.3.21) into (3.0.1) yields

$$\frac{d\sigma_{i\to f}(E)}{d\Omega_{k_f}} = \frac{2\pi}{\hbar F_i}\sum_{dd'}\frac{\langle\Phi_f|RH_{er}Q|\Phi_d\rangle\langle\Phi_d|QH_{er}R|\Phi_i\rangle}{E-E_d-\Delta E_d^R+\frac{i}{2}\Gamma_d^R} \times\frac{\langle\Phi_f|RH_{er}Q|\Phi_{d'}\rangle^*\langle\Phi_{d'}|QH_{er}R|\Phi_i\rangle^*}{E-E_{d'}-\Delta E_{d'}^R-\frac{i}{2}\Gamma_{d'}^R}\rho_f\ . \tag{3.4.1}$$

Here, the complex energy variable z has been replaced by the total energy E of the system, which is given by the sum of the photon energy and the energy of the initial state of the ion

$$E = \hbar\omega + E_i = E_{phot} + E_i\ . \tag{3.4.2}$$

Applying once again the *isolated resonances approximation*, we neglect the non-diagonal elements of the double sum

$$\frac{d\sigma_{i\to f}(E_{phot})}{d\Omega_{k_f}} = \frac{2\pi}{\hbar F_i}\sum_{d}\frac{|\langle\Phi_f|RH_{er}Q|\Phi_d\rangle|^2\,|\langle\Phi_d|QH_{er}R|\Phi_i\rangle|^2}{(E_{phot}-E_d+E_i)^2+\frac{\Gamma_d^{R\,2}}{4}}\rho_f\ . \tag{3.4.3}$$

Equation (3.4.2) has been used in the above formula.

We now proceed to calculate explicit expressions for the two squared matrix elements in the numerator. We start first with $|\langle\Phi_f|RH_{er}Q|\Phi_d\rangle|^2$, which describes spontaneous emission of a photon as the system evolves from the bound atomic, zero-photon state $|\Phi_d, 0\rangle$ to the bound atomic, 1-photon state $|\Phi_f, \lambda\vec{k}\rangle$. Now we give explicitly the total number of photons present in the field and write

$$\begin{aligned}|Q\Phi_d\rangle &= |\Phi_d\rangle = |d, J_d, M_{J_d}\rangle|n\rangle\,,\\ |R\Phi_f\rangle &= |\Phi_f\rangle = |f, J_f, M_{J_f}\rangle|n+1\rangle\,.\end{aligned} \tag{3.4.4}$$

Following the calculation in [1], for simplicity we give the 1-electron, 1-polarization, single-mode form of (3.1.8):

$$H'_{er} = \frac{e}{m}\sqrt{\frac{2\pi\hbar}{V\omega}}\left[a(\vec{p}\cdot\vec{\epsilon})e^{i\vec{k}\vec{r}} + a^\dagger(\vec{p}\cdot\vec{\epsilon})e^{-i\vec{k}\vec{r}}\right], \tag{3.4.5}$$

because when applying Fermi's Golden Rule we will see that the sum over relevant modes $\vec{k}$ and the extension to a many-electron atom can be carried

out with a sum $\sum_i$ over all electrons. The polarization λ of the emitted photon will be treated later on. In H'_{er}, the term with the annihilation operator a is not relevant, since we consider an emission event. Furthermore, first we apply the electric dipole (E1) approximation, e.g. we keep only the first term of the multipole expansion of $e^{i\vec{k}\vec{r}}$, namely, 1. By using the Heisenberg equation of motion

$$[\vec{r}, H_0] = i\hbar\frac{d\vec{r}}{dt} = i\hbar\frac{\vec{p}}{m}\,, \tag{3.4.6}$$

introducing the electric dipole operator $\vec{d} = -e\vec{r}$ in the spherical basis with the index $q = -1, 0, 1$ and applying the Wigner-Eckart theorem, one obtains

$$\begin{aligned}\langle\Phi_f|RH'_{er}Q|\Phi_d\rangle =& i\sqrt{\frac{2\pi\hbar\omega_{res}(n+1)}{V}}\frac{\langle f, J_f||\hat{d}||d, J_d\rangle}{\sqrt{2J_f+1}} \\ &\times\sum_q\langle J_d, M_{J_d}, 1, q|J_f, M_{J_f}\rangle\epsilon_q\,.\end{aligned} \tag{3.4.7}$$

Here, $\hat{d}$ is the dipole operator[11] and $\omega_{res} = E_{di}/\hbar$ with the energy separation of the two states E_{di}. Note the $\sqrt{n+1}$ factor following from the definitions (3.4.4).[12] $\langle f, J_f||\hat{d}||d, J_d\rangle$ is the so-called *reduced* matrix element, free of any dependence on the quantum numbers M_J and is real, like the rest of the terms except i. Now we take the modulus square of expression (3.4.7):

$$\begin{aligned}\left|\langle\Phi_f|RH'_{er}Q|\Phi_d\rangle\right|^2 =& \frac{2\pi\hbar\omega_{res}(n+1)}{V}\frac{\left|\langle f, J_f||\hat{d}||d, J_d\rangle\right|^2}{2J_f+1} \\ &\times\left(\sum_q\langle J_d, M_{J_d}, 1, q|J_f, M_{J_f}\rangle\epsilon_q\right)^2\,,\end{aligned} \tag{3.4.8}$$

then multiply by 2 for the two polarizations available and choose $\vec{\epsilon}$ along the quantization axis z, e.g. $e_{q=0} = 1$, $e_{q=\pm1} = 0$ (spherical basis). Additionally, for spontaneous emission, $n = 0$, since there is no active photon in the state $|\Phi_d\rangle$. We also sum over all possible ground states M_{J_f} and average over the excited state sublevels M_{J_d}. The two sums $\sum_{M_{J_f}}$ and $\sum_{M_{J_d}}$ apply then only to the squared M_J-dependent matrix element

$$\sum_{M_{J_f}}\sum_{M_{J_d}}\langle J_d, M_{J_d}, 1, 0|J_f, M_{J_f}\rangle^2\,, \tag{3.4.9}$$

[11] $\hat{d}$ is a vector, i.e. a rank-1 tensor, which accounts for the 1 in the last matrix element of (3.4.7).

[12] $\langle n+1|a^\dagger|n\rangle = \sqrt{n+1}\langle n+1|n+1\rangle = \sqrt{n+1}\,.$

which is equal to $(2J_f+1)/3$, expressing the isotropy of space (equally probable photon emission in every direction). Thus finally[13]:

$$\left|\langle\Phi_f|RH'_{er}Q|\Phi_d\rangle\right|^2 = \frac{4\pi\hbar\omega_{res}}{3V}\frac{\left|\langle f,J_f||\hat{d}||d,J_d\rangle\right|^2}{2J_d+1} \tag{3.4.10}$$

If one inserts this result into Fermi's Golden Rule for emission and integrates over the solid angle $d\Omega$, one obtains the radiative decay rate between fine structure levels[14]

$$A^{FS}_{d\to f} = \frac{4\omega^3_{res}}{3\hbar c^3}\frac{\left|\langle f,J_f||\hat{d}||d,J_d\rangle\right|^2}{2J_d+1}\,. \tag{3.4.11}$$

We can thereby express $\left|\langle f,J_f||\hat{d}||d,J_d\rangle\right|^2$ in terms of $A^{FS}_{d\to f}$:

$$\left|\langle f,J_f||\hat{d}||d,J_d\rangle\right|^2 = \frac{3\hbar c^3}{4\omega^3_{res}}(2J_d+1)A^{FS}_{d\to f} \tag{3.4.12}$$

The purpose of this will soon become clear to the reader. We now proceed in a similar way for $|\langle\Phi_d|QH_{er}R|\Phi_i\rangle|^2$, the squared matrix element for the resonant absorption of only one photon. This time the $a^\dagger$-term in (3.4.5) does not contribute and the electric dipole approximation still holds. After the use of the Wigner-Eckart theorem and, say, for z-polarized light ($q=0$), we have

$$\langle\Phi_d|QH'_{er}R|\Phi_i\rangle = -i\sqrt{\frac{2\pi\hbar\omega_{res}n}{V}}\cdot\frac{\langle d,J_d||\hat{d}||i,J_i\rangle}{\sqrt{2J_d+1}}\langle J_i,M_{J_i},1,0|J_d,M_{J_d}\rangle\,. \tag{3.4.13}$$

One can express the number n of photons in the mode by the electric field amplitude[15]:

$$n = \frac{V\mathcal{E}_0^2}{8\pi\hbar\omega_{res}} \tag{3.4.14}$$

so that after summation over M_{J_d}, averaging over M_{J_i} and due to isotropy:

$$\left|\langle\Phi_d|QH'_{er}R|\Phi_i\rangle\right|^2 = \frac{1}{12}\frac{\left|\langle d,J_d||\hat{d}||i,J_i\rangle\right|^2\mathcal{E}_0^2}{2J_i+1}\,. \tag{3.4.15}$$

The absorption rate for n photons $A^{FS,n}_{i\to d}$ is related to the stimulated decay

[13] In case of a dimension check of the formula, note that $\left|\langle f,J_f||\hat{d}||d,J_d\rangle\right|^2$ has the dimension energy·volume due to choice of $1/(4\pi\epsilon_0)\equiv 1$ in the definition of H_0, [1], p. 138

[14] $A^{FS}_{d\to f}$ has the dimension 1/time.

[15] The time-averaged magnitude of the Poynting vector for an electromagnetic plane wave is $\frac{\mathcal{E}_0^2 c}{8\pi}$ under the convention $1/(4\pi\epsilon_0)\equiv 1$.

rate for n photons $A^{FS,n,st}_{d\to i}$ according to the principle of detailed balance

$$A^{FS,n}_{i\to d} = \frac{2J_d+1}{2J_i+1} A^{FS,n,st}_{d\to i} \,. \tag{3.4.16}$$

For the moment however let us consider the spontaneous decay rate $A^{FS}_{d\to i}$ and write in analogy to (3.4.12):

$$\left|\langle d, J_d||\hat{d}||i, J_i\rangle\right|^2 = 8\pi \frac{3\hbar c^3}{4\omega^3_{res}} (2J_d+1) A^{FS}_{d\to i} = 8\pi \frac{3\hbar c^3}{4\omega^3_{res}} (2J_i+1) A^{FS}_{i\to d} \,, \tag{3.4.17}$$

with the absorption rate per photon $A^{FS}_{i\to d}$. The above equality is another manifestation of the principle of detailed balance in the case of one photon, e.g. $n = 1$. The factor 8π is present, because for absorption the rate has to be *averaged* rather than integrated over the solid angle $d\Omega$ and the 2 possible polarizations λ.

Before we insert (3.4.10) and (3.4.15) into (3.4.3), we give the expressions for the density of states of the final states ρ_f and the flux of incoming photons F_i. ρ_f in this case is the density of the photon states:

$$\rho_f(E_{phot}) = \frac{dN}{dE} = \frac{V}{(2\pi)^3} \frac{E^2_{phot}}{\hbar^3 c^3} \tag{3.4.18}$$

dN is the number of photons of energy E_{phot} in a given differential volume of phase space

$$dN = \frac{d^3x\, d^3p}{(2\pi\hbar)^3} \,. \tag{3.4.19}$$

The flux[16] is related to the electric field amplitude

$$F_i = \frac{1}{\hbar\omega_{res}} \frac{c\mathcal{E}^2_0}{8\pi} \,. \tag{3.4.20}$$

We finally insert (3.4.10), (3.4.15), (3.4.18) and (3.4.20) into (3.4.3) and consider the transition to one specific level d:

$$\begin{aligned} \frac{d\sigma_{i\to d\to f}(E_{phot})}{d\Omega_{k_f}} =& \frac{4\pi^2}{9} \frac{E^2_{di}\omega^2_{res}}{\hbar^2 c^4} \frac{\left|\langle f, J_f||\hat{d}||d, J_d\rangle\right|^2 \left|\langle d, J_d||\hat{d}||i, J_i\rangle\right|^2}{(2J_d+1)(2J_i+1)} \\ & \times \frac{L(E_{phot}; E_{di}, \Gamma^R_d)}{\Gamma^R_d} \end{aligned} \tag{3.4.21}$$

[16] Dimension: photons/(area·time).

with $E_{di} = \hbar\omega_{res}$ having been introduced as the argument of $\rho_f(E_{phot})$ and the energy-normalized Lorentzian line shape function

$$L(E_{phot}; E_{di}, \Gamma_d^R) = \frac{\Gamma_d^R/2\pi}{(E_{phot} - E_{di})^2 + \frac{\Gamma_d^{R\,2}}{4}}\,, \tag{3.4.22}$$

where $E_{di} = E_d - E_i$. We now make use of (3.4.12) and (3.4.17) in (3.4.21) and proceed to the total cross section by *averaging* over the incoming photon directions, polarizations and magnetic quantum numbers M_{J_i}, as well as integrating over the directions of the outgoing photons, summing over their polarizations and summing over M_{J_f}. Note however that all these have been already carried out implicitly in the derivation of (3.4.12) and (3.4.17), thus

$$\sigma_{i\to d\to f}(E_{phot}) = \frac{\pi^2 c^2 \hbar^3}{E_{di}^2} A_{i\to d}^{FS} L(E_{phot}; E_{di}, \Gamma_d^R)\, \frac{\hbar A_{d\to f}^{FS}}{\Gamma_d^R}\,. \tag{3.4.23}$$

The last term $\frac{\hbar A_{d\to f}^{FS}}{\Gamma_d^R}$ is the so-called *branching ratio*, which in this case is equal[17] unity, since there is only one possible transition channel, the one between the degenerate states $|d, J_d\rangle$ and $|f, J_f\rangle$.

In the actual presence of n photons in the mode, the total emission rate is given by $A_{d\to i}^{FS,n+1} = A_{d\to i}^{FS,n,st} + A_{d\to i}^{FS}$. Despite this fact, the branching ratio remains still the same as in the one-photon case of spontaneous decay.

We note here that even though the above final formula has been derived in the case of electric dipole transitions, one may get the same result for magnetic dipole (M1) transitions. This is due to the fact that the radiative rates in the M1 case have the same form as their E1 counterparts, with the exception that the electric dipole operator needs to be substituted by the electronic magnetic dipole operator.

[17] Due to the notation in [1], it is in this special case: $\Gamma = \hbar A$.

Chapter 4

Hyperfine Structure

Formula (3.4.23) has been derived in a general way for the transitions between states with $(2J+1)$ degeneration characterized by the total angular momentum quantum number J. However, in the framework of this thesis the calculation of the total cross section for transitions between levels belonging to the Zeeman-split hyperfine levels is aimed for. Therefore, some modifications concerning the level energies and transition rates are undertaken in the above-mentioned formula. Furthermore, the energy levels E_d and E_i are given in explicit form.

4.1 Transition Rates

The transition rates $A^{FS}_{i\to d}$ and $A^{FS}_{d\to f}$ for the fine-structure splitting, which have been used so far, have to be replaced by the decay rates $A^{hfs}_{i\to d}$ and $A^{hfs}_{d\to f}$ between two Zeeman-split levels of the hyperfine structure. Additionally, the energy levels are not considered degenerate anymore; the principle of detailed balance reduces to

$$A^{hfs}_{i\to d} = A^{hfs}_{d\to i}\,. \tag{4.1.1}$$

We obtain thus from (3.4.23)

$$\sigma_{i\to d\to f}(E_{phot}) = \frac{\pi^2 c^2 \hbar^4}{E^2_{di}} A^{hfs}_{d\to i} L(E_{phot}; E_{di}, \Gamma^R_d)\, \frac{A^{hfs}_{d\to f}}{\Gamma^R_d}\,. \tag{4.1.2}$$

Note that for the radiative width Γ^R_d holds:

$$\Gamma^R_d = h \sum_f A^{hfs}_{d\to f} \tag{4.1.3}$$

since $i \equiv f$ does not hold necessarily, so that all possible final states of the decay have to be considered. As opposed to the relation $\Gamma_d^R = hA_{d\to i}^{FS}$ of Section 3.4, here it is summed over all possible decay rates $A_{d\to f}^{hfs}$ between *Zeeman components of the hyperfine splitting* with quantum numbers F and M_F, which is given by [14]

$$A_{d\to f}^{hfs} = (2F_d+1)(2F_f+1)\overbrace{\begin{pmatrix} F_f & J_{phot} & F_d \\ -M_{F_f} & M_{F_f}-M_{F_d} & M_{F_d}\end{pmatrix}^2}^{\zeta} \times \underbrace{\begin{Bmatrix} J_f & F_f & I \\ F_d & J_d & J_{phot}\end{Bmatrix}^2}_{\eta} A_{d\to f}^{FS}\,. \tag{4.1.4}$$

Here, I is the nuclear spin quantum number and $A_{d\to f}^{FS}$ is the fine-structure decay rate between electronic states with quantum number J introduced in Section 3.4. This value is delivered by the OSCL program of GRASP. The factors ζ and η denote the square of the *Wigner* $3j$*-symbol* and *Wigner* $6j$*-symbol* respectively[1]. The quantum numbers involved fulfill among others the triangular inequalities

$$|F_f - 1| \le F_d \le F_f + 1 \tag{4.1.5}$$

and

$$-J_{phot} \le M_{F_f} - M_{F_d} \le J_{phot}\,. \tag{4.1.6}$$

Since J_{phot}, the photon angular momentum, is equal to 1, the above relations express the selection rules

$$\begin{aligned} \Delta F &= 0, \pm 1\,, \\ \Delta M_F &= 0, \pm 1\,. \end{aligned} \tag{4.1.7}$$

If these are not satisfied, the $3j$- and $6j$-symbols are equal to 0, i.e. the M1 transition between those states is forbidden.

$\sigma_{i\to d\to f}$ is the total cross section for exactly *one* transition channel from state i to d and finally to state f. However, since we aim to obtain the cross section for all possible transitions, we have to sum over all possible states i,d,f. We perform first the summation over f, since there is only one term that depends on it, namely, $A_{d\to f}^{hfs}$. This gives the result[2]

$$\sum_f A_{d\to f}^{hfs} = \frac{1}{2J_d+1} A_{d\to i}^{FS} = \frac{\Gamma_d^R}{h}\,. \tag{4.1.8}$$

[1] See [17], p. 1054, 1061.
[2] See Appendix C.

This leads from formula (4.1.2) to the final expression for the total cross section of a transition under photon absorption from an initial state i to an excited, intermediate state d, followed by a radiative decay towards all possible final states f

$$\sigma_{i\to d}(E_{phot}) = 2\frac{\pi^3 c^2 \hbar^3}{E_{di}^2} A_{d\to i}^{hfs} L(E_{phot}; E_{di}, \Gamma_d^R)\,, \tag{4.1.9}$$

with

$$\Gamma_d^R = \frac{h}{2J_d+1} A_{d\to i}^{FS}\,. \tag{4.1.10}$$

When plotting the spectrum for transitions involving different initial and excited states, i.e. a superposition of peaks, the remaining summation over i and d can be done numerically, e.g. by a *Mathematica* code.

4.2 Level Energies

The level energies include the interaction energies of the hyperfine splitting and the Zeeman splitting of the components of the hyperfine structure.

4.2.1 Hyperfine interaction

The term $\sum_{i=1}^{n_e} H_{hfs}(\vec{r_i})$ in (3.1.2) describing the hyperfine interaction between the electrons and the electromagnetic multipole moments of the nucleus may be represented as a multipole expansion [10, 12]:

$$\sum_{k\geq 1} T^{(k)} \cdot M^{(k)} \tag{4.2.1}$$

where $T^{(k)}$ and $M^{(k)}$ are spherical tensor operators of rank k in the electronic and nuclear spaces, respectively. The multipolarity $k = 1$ corresponds to the magnetic dipole interaction and $k = 2$ to the electric quadrupole interaction. Higher-order terms are small enough to be neglected. The nuclear tensor operators are related to the conventional nuclear magnetic dipole moment μ_I and electric quadrupole moment Q_I in the following way:

$$\mu_I = \langle \Gamma_I I M_I | M_0^{(1)} | \Gamma_I I M_I \rangle, \tag{4.2.2}$$

$$\frac{1}{2} Q_I = \langle \Gamma_I I M_I | M_0^{(2)} | \Gamma_I I M_I \rangle, \tag{4.2.3}$$

where the state of the nucleus is denoted by $|\Gamma_I I M_I\rangle$ in analogy to the atomic state function notation in Chapter 2 and is assumed to be independent of the electronic states. The nuclear and electronic angular momenta, $\vec{I}$ and $\vec{J}$, respectively, are coupled to a total angular momentum $\vec{F} = \vec{I} + \vec{J}$. The matrix elements of the magnetic dipole and electrical quadrupole interactions are

$$W_{M1}(J, J') = \langle \Gamma_I \Gamma_J I J F M_F | T^{(1)} \cdot M^{(1)} | \Gamma_I \Gamma_J J' F M_F \rangle \tag{4.2.4}$$

$$W_{E2}(J, J') = \langle \Gamma_I \Gamma_J I J F M_F | T^{(2)} \cdot M^{(2)} | \Gamma_I \Gamma_J J' F M_F \rangle \,, \tag{4.2.5}$$

where

$$|\Gamma_I \Gamma_J I J F M_F\rangle = \sum_{M_I M_J} C\left(IJF; M_I M_J M_F\right) |\Gamma_I I M_I\rangle |\Gamma_J J M_J\rangle \tag{4.2.6}$$

denotes the coupled wave function of the total system composed of the nucleus and the electrons. After the factorization of the nuclear and electronic terms, the diagonal matrix elements can be given by [10, 12]

$$W_{M1}(J, J) = \frac{1}{2} A_J C \,, \tag{4.2.7}$$

$$W_{E2}(J, J) = B_J \frac{\frac{3}{4} C(C+1) - I(I+1) J(J+1)}{2I(2I-1)J(2J-1)} \,. \tag{4.2.8}$$

Here, $C = F(F+1) - J(J+1) - I(I+1)$ and A_J, B_J are the hyperfine interaction constants, which are calculated by the HFS92 program written as an extension to GRASP after empirical values of the nuclear magnetic moments have been inserted by the user. Since both constants have the dimension 1/time, the resulting hyperfine energy splitting due to magnetic dipole and electrical quadrupole interaction considering only diagonal elements is given by $hW_{M1}(J, J)$ and $hW_{E2}(J, J)$, respectively.

4.2.2 Zeeman splitting of the hyperfine structure components

The energy shift due to the Zeeman interaction $-\vec{\mu_F}\vec{B}$ in first-order perturbation theory is given by [14]

$$\Delta E^{Zeem} = \mu_B g_F B M_F \,, \tag{4.2.9}$$

where $\mu_B = \frac{e\hbar}{2m_e}$ is the Bohr magneton and g_F the g factor for a hyperfine niveau F. The latter is given by the expression [14]:

$$g_F = g_J \frac{F(F+1) + J(J+1) - I(I+1)}{2F(F+1)} \,, \tag{4.2.10}$$

with g_J being the g factor for a fine-structure level, defined by the magnetic moment $\vec{\mu}_J$ of an atom in state $|JM_J\rangle$ as

$$\vec{\mu}_J = -g_J \mu_B \vec{J}. \tag{4.2.11}$$

g_J, as computed by the GFACTOR2001 program [13], comprises one important QED correction: the interaction of the free electron with the quantized electromagnetic vacuum. In principle, this is still an approximation since further corrections for bound electrons should be taken into consideration. However, the latter would extend beyond the precision of the actual experiments and our intended theoretical accuracy, and will not be taken into account.

Finally, the overall expression for the energy level $E_{i/d}$ up to the Zeeman splitting of the hyperfine structure results to

$$E_{i/d} = E_{J_{i/d}} + hW_{M1}(J_{i/d}, J_{i/d}) + hW_{E2}(J_{i/d}, J_{i/d}) + \Delta E^{Zeem}. \tag{4.2.12}$$

This means that the quantity E_{di} in the Lorentzian function of expression (4.1.9) is given by

$$\begin{aligned} E_{di} = {} & E_{J_d} - E_{J_i} + hW_{M1}(J_d, J_d) - hW_{M1}(J_i, J_i) \\ & + hW_{E2}(J_d, J_d) - hW_{E2}(J_i, J_i) + \Delta E^{Zeem}_{M_{F_d}} - \Delta E^{Zeem}_{M_{F_i}}. \end{aligned} \tag{4.2.13}$$

Note that the fine-structure energies $E_{J_{i/d}}$ are calculated according to the MCDF theory described in Chapter 2.

An overview of the energy levels, splittings and transition rates is given in figures 4.1 and 4.2. Transitions within one group of the $2M_F+1$ Zeeman-split levels or even between two hyperfine levels that belong to the same J have not been taken into account, as those have frequencies in the microwave- or radio frequency-range with negligible transition rates. This is justified by the $A^{hfs}_{d\to f} \propto \omega^3$-dependence of transition rates [12].

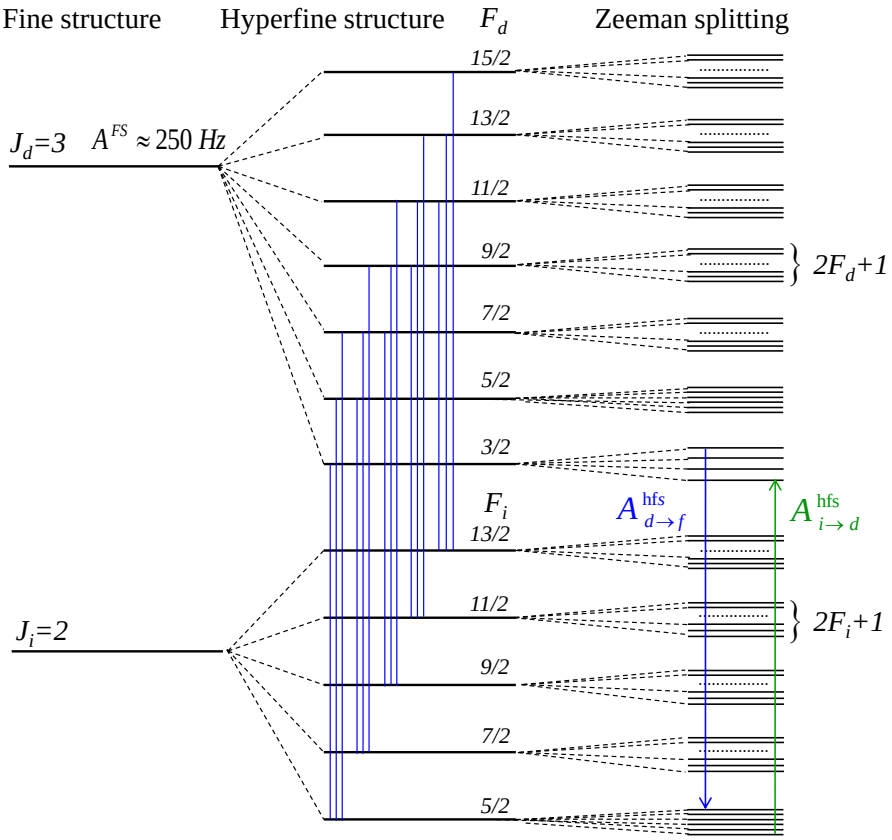

Figure 4.1: Schematic diagram of the $J = 2, 3$ energy levels of the peel subshell configuration $3d^4$ illustrating the fine, hyperfine and Zeeman splitting (not to scale). 410 transitions between Zeeman states with different J are allowed according to the selection rules (4.1.7), out of which only 2 have been depicted. The 12 transitions between $|J_d = 3, F_d = 3/2, M_{F_d}\rangle$ and $|J_i = 2, F_i = 5/2, M_{F_i}\rangle$ are given explicitly in Figure 4.2.

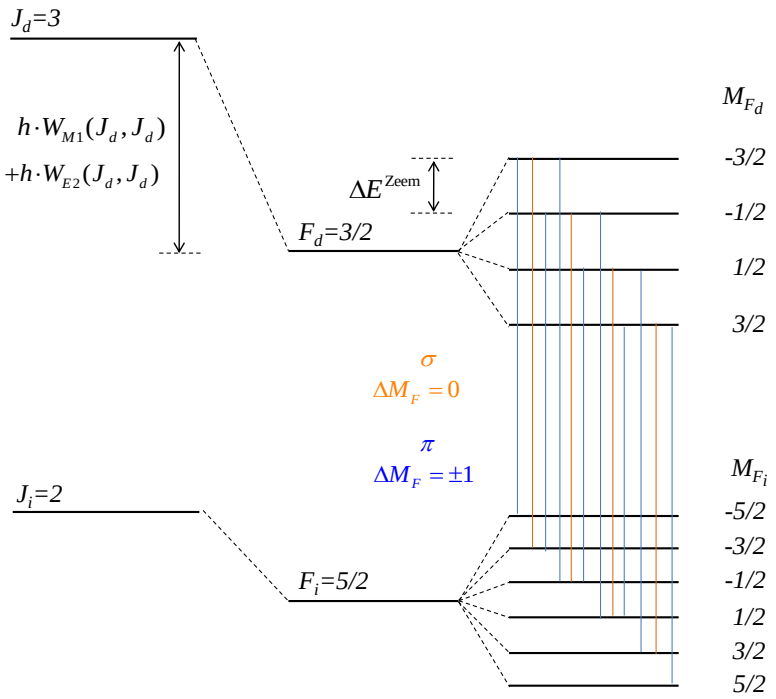

Figure 4.2: Allowed magnetic dipole transitions between $|J_d = 3, F_d = 3/2\rangle$ and $|J_i = 2, F_i = 5/2\rangle$. Note the inversion of the Zeeman levels is caused by the negative sign of g_F. σ and π refer to the orthogonal (to the direction defined by the magnetic field) and parallel polarization of the emitted photon. The proportions of the Zeeman splittings in the figure correspond to the real values.

Chapter 5

Results

This chapter is composed of two parts. In the first, a series of multiconfiguration Dirac-Fock calculation results are presented. These have been crucial in determining the accuracy of the numerical codes employed as well as the magnitude of several contributions such as QED and nuclear corrections. Furthermore, a comparison of results carried out with two different types of configuration expansions point out the necessary adjustments of the calculation. In the second part, a formula for the Doppler-broadened cross section σ^D is derived, in order to obtain predictions with respect to the experiment, which is bound with line broadening. Finally, σ^D is plotted with different parameters and the respective spectra are discussed.

Table 5.1: Numerical values of the fine structure energy E_J, M1 transition rate between fine structure levels, hyperfine interactions constants A_J, B_J and g factor for the fine structure g_J obtained with an expansion up to $n = 4$ for the lowest $J = 2, 3$ levels of the $3d^4$ subshell in $^{209}Bi^{61+}$.

J	E_J (eV)	$A^{FS}_{d\to f}$ (Hz)	A_J (GHz)	B_J (GHz)	g_J
3	−484570.73	250.14900	80.6718	−29.7589	1.06983
2	−484574.38		61.7162	−36.6734	1.15729

5.1 Choice of the Expansion Size

An issue that arises while generating the list of the configuration state functions is the choice of the appropriate expansion size. From a comparison of two calculations, the one extending to $n = 3$ and the other to $n = 4$, the results presented in table 5.2 have been obtained.

Table 5.2: Calculation results for expansions with $n = 3$ and $n = 4$.

n	3	4
$E_{J_d} - E_{J_i}$ (eV)	3.64374	3.65820
$A^{FS}_{d\to f}$ (Hz)	300.68170	250.14900
A_{J_d} (GHz)	80.8133	80.6718
A_{J_i} (GHz)	61.8188	61.7162
B_{J_d} (GHz)	−29.8566	−29.7589
B_{J_i} (GHz)	−36.7696	−36.6734

Configurations with $J = 2$, $J = 3$ as well as single and double substitutions have been considered. All the relative deviations are under 1%. Concerning the value of $E_{J_d} - E_{J_i}$ it should be mentioned that obtaining a highly accurate value is not within the aims of this work, since precise values are given in Ref. [4]. Moreover, the same tendency of increasing fine structure energy splittings with higher n as mentioned in [4] has been observed.
The hyperfine interaction constants A_j, B_J have been determined with an accuracy that presently lies beyond experimental precision, as a discrepancy of 0.1 GHz corresponds to $\approx 0.4\,\mu$eV, which is far less that the actual experimental resolution as it is discussed further below. Thus since it is expected that a configuration symmetry list going up to $n = 5$ will provide the same order of magnitude in the improvement of the above values, the $n = 4$ expansion has been considered sufficient and has been used throughout the calculations of this work.
For the calculation of the decay rate $A^{FS}_{d\to f}$ between fine structure levels magnetic dipole (M1) transitions have been considered in order to compare them with the values presented in [4]. Note that the $A^{FS}_{d\to f}$ value for $n = 3$ is subject to a deviation of $\approx 27\%$ relative to the value 236.79 Hz in [4], which also speaks for a $n = 4$ expansion where the relative deviation lies at 5%.

5.2 Multipole Expansion of the Electromagnetic Field

For the calculation of the fine structure energy levels and transition rates magnetic dipole transitions have been considered. The expansion of the electromagnetic plane waves of the radiation field consists of the following terms[1]:

$$\mathbf{M1}+\mathrm{E1}+\mathbf{E2}+\mathrm{M2}+\mathbf{M3}+\mathrm{E3}+\mathbf{E4}+\mathrm{M4}+\mathbf{M5}+\mathrm{E5}+\dots\,,$$

where "ML" refers to magnetic and "EL" to electric type, respectively. $L = 1$ corresponds to dipole, $L = 2$ to quadrupole, $L = 3$ to octupole transitions etc.
The parity selection rule holds:

$$\pi_i\pi_d = (-1)^L \quad \text{for electric dipole transitions,} \tag{5.2.1}$$

$$\pi_i\pi_d = (-1)^{L+1} \quad \text{for magnetic dipole transitions.} \tag{5.2.2}$$

In our case we have $\pi_i = \pi_d$, e.g. $\pi_i\pi_d = +1$.
Additionally the following total angular momentum selection rules hold:

$$|J_d - J_i| \leq L \leq J_d + J_i\,, \tag{5.2.3}$$

or in our case:

$$1 \leq L \leq 5\,. \tag{5.2.4}$$

Thus only the transitions corresponding to the terms in bold are allowed.
A calculation with the "oscl92" executable[2] of GRASP for $n = 4$, $J = 2 \leftrightarrow J = 3$ level transition of the $3d^4$ subshell yielded $A^{FS}_{d\to f} = 250.14900\,\mathrm{Hz}$ and $A^{FS}_{d\to f} = 3.9 \times 10^{-4}\mathrm{Hz}$ for M1 and E2 transitions respectively. The latter corresponds to a lifetime of $\approx 40\,\mathrm{min}$, which can be considered as an infinitely long time interval for interatomic processes. As higher multipolarity transitions are expected to be of even less importance than E2, the calculations have been restricted to M1 transitions.

5.3 Comparative, Hydrogenlike Calculation

In order to test the numerical results of the computations with GRASP, a calculation of the hyperfine splitting of hydrogen like bismuth $^{209}\mathrm{Bi}^{82+}$ has

[1] See e.g. [12].
[2] For a brief description of GRASPs executables see appendix A.

been performed and compared with the values that were obtained with an analytical formula for the hyperfine splitting of a one-electron ion given e.g. in [21][3]. The results are summarized in tables 5.3 and 5.4, showing that the numbers are in agreement within our required degree of accuracy.
Note that for the hyperfine splitting energies calculated numerically with GRASP, only the magnetic dipole interaction $W_{M1}(J,J)$ (see Section 4.2) has been considered in these test studies with hydrogenic systems. However, for the rest of the calculations in this work, both magnetic dipole and electrical quadrupole interactions have been taken into account since the corresponding interaction constants, A_J and B_J respectively, are of the same order of magnitude, as it can be seen in table 5.1.
Additionally the g factor values for the Zeeman splitting of the fine structure obtained from the hydrogenlike numerical calculation have been compared with the analytical formula for a point like nucleus in the one-electron Dirac theory [23]:

$$g_D = \frac{\kappa}{j(j+1)}\left(\kappa\frac{\gamma+n-|\kappa|}{\sqrt{(\gamma+n-|\kappa|)^2+(\alpha Z)^2}}-\frac{1}{2}\right), \tag{5.3.1}$$

where α is the fine structure constant, Z the nuclear charge number, n denotes the principal quantum number, $\kappa=(-1)^{j+l+\frac{1}{2}}(j+1/2)$ is the Dirac angular momentum quantum number and j represents the relativistic total angular momentum quantum number. Furthermore, $\gamma=\sqrt{\kappa^2-(\alpha Z)^2}$. The results are summarized in table 5.5. The values are in agreement up to 7 and 8 significant digits for $j=\frac{3}{2}, j=\frac{5}{2}$ respectively.

Table 5.3: Values for hyperfine splitting obtained numerically, compared to the exact analytical result for $n=3$, $l=3$, $j=3/2$.

F	$\Delta E_{hfs}^{\text{exact}}$ (meV)	hW_J^{GRASP} (meV)
3	−7.8374	−7.83738
4	−4.0374	−4.03743
5	0.7125	0.71248
6	6.4124	6.41240

[3]Formula (1) of the cited paper was implemented using CODATA 2010 values. Relativistic but no nuclear or QED effects were taken into account, e.g. $\epsilon\equiv 0$ (point like nucleus), $\delta\equiv 0$ (no Bohr-Weisskopf effect), $x_{rad}\equiv 0$.

Table 5.4: Values for hyperfine splitting obtained numerically, compared to the exact analytical result for $n = 3$, $l = 3$, $j = 5/2$.

F	$\Delta E_{hfs}^{\text{Shab}}$ (meV)	W_J^{GRASP} (meV)
2	−5.0230	−5.02300
3	−3.9271	−3.92707
4	−2.4658	−2.46583
5	−0.6393	−0.63929
6	1.5526	1.55256
7	4.1097	4.10973

Table 5.5: Fine structure g factor values from Dirac theory and from numerical GRASP calculation for the $3d$ electron in hydrogenlike $^{209}Bi^{82+}$.

j	g_D	g_J^{GRASP}
3/2	0.777561435828744	0.7775614276
5/2	1.178819140473812	1.1788191462

5.4 QED and Nuclear Effects

As mentioned in the introduction of this work, quantum field theory is needed to handle theoretically highly charged ions. QED corrections like Breit interaction, self-energy and vacuum polarization, as well as nuclear motional corrections (normal and specific mass shift[4]) have been added from GRASPs program "rci92" to the Dirac-Coulomb Hamiltonian *a posteriori*. This means that the radial functions are not altered, merely the solution of the eigenvalue problem for the expansion coefficients is repeated by diagonalizing the modified Hamiltonian matrix, which includes the above-mentioned effects.

The influence of these corrections is relevant: Within a calculation up to $n = 4$, considering configurations with $J = 2, 3$, single and double substitutions (635 CSFs), an optimized level (OL) procedure with and one without QED and nuclear corrections have been compared. The results are given in table 5.6.

[4]See [19], p. 264.

Table 5.6: Numerical data showing the magnitude of QED and nuclear recoil effects.

Corrections	$E_{J_d} - E_{J_i}$ (eV)	$A^{FS}_{d\to i}$ (Hz)	g_{J_d}	g_{J_i}
included	3.658	250.149	1.06983	1.15729
not included	3.816	280.540	1.06967	1.15703

The relative deviation in the difference of the fine structure splitting lies at 4%, in the radiative decay rate between fine structure levels $A^{FS}_{d\to i}$ at 12%, bringing the value including QED and mass shift corrections significantly closer to the value 236.79 Hz given in [4]. The deviation in the g_J values lies in the 0.01% regime; the same is thus expected for the Zeeman splitting energies.
Note that for a correct treatment of QED effects on the HFS and Zeeman corrections, the corresponding Feynman diagrams shall be rigorously implemented. These would influence the results with a relative contribution on the order of the fine-structure constant $\alpha \approx 1/137$, i.e. approximately on the 1% level. Thus we can neglect these terms at the level of accuracy we are aiming at for an informative comparison with anticipated experimental results.

5.5 Doppler Broadening

In the actual experiment, the spectral lines are subject to Doppler broadening, which sets limitations to the practical resolution of the observed spectra. If ω_{res} is the resonant frequency of the atom in its rest frame, it follows from the Maxwellian velocity distribution due to thermal motion of the atoms that the absorbtion cross section has a Gaussian profile [5]:

$$G(\omega) = \frac{c}{\omega_{res}\sqrt{\pi}} e^{-\frac{c^2}{u^2\omega^2_{res}}(\omega-\omega_{res})^2} \tag{5.5.1}$$

or depending on the photon energy E_{phot}:

$$G(E_{phot}) = \frac{\hbar c}{E_{res}\sqrt{\pi}} e^{-\frac{c^2}{u^2 E^2_{res}}(E_{phot}-E_{res})^2} \tag{5.5.2}$$

with $u = \sqrt{2k_BT/M}$ being the most probable speed.
The radiative decay rate between fine structure levels, $A^{FS}_{d\to f}$, amounts to 250.14900 Hz. According to Heisenberg´s uncertainty relation this corresponds to a line broadening or radiative width of the state $|\Phi_d\rangle$:

$$\Gamma^R_d = hA^{FS}_{d\to f} = 1.4779044 \times 10^{-13}\,\text{eV} \tag{5.5.3}$$

This low order of magnitude of this value confirms the validity of the isolated resonances approximation assumed along the derivation of the cross section formula. Taking into account that the energy difference between the $3d$ states $J_i = 2$ and $J_d = 3$ lies at $\approx 3.6\,\text{eV}$, one can approximate the Lorentzian-like cross section of each of the 410 allowed transitions by a delta function.
In order to obtain the expected observed spectrum under a given resolution, the cross section with the natural line width has to be convoluted with the Gaussian line shape function involving the Doppler broadening:

$$\sigma_{i\to f}(E_{phot}) \propto \int_0^\infty L(\tilde{E}; E_{res}, \Gamma^R_d) \cdot Ne^{-\frac{(E_{phot}-\tilde{E})^2}{2\sigma^2}} d\tilde{E} \tag{5.5.4}$$

$$\approx \int_0^\infty \delta(\tilde{E} - E_{res}) \cdot Ne^{-\frac{(E_{phot}-\tilde{E})^2}{2\sigma^2}} d\tilde{E} \tag{5.5.5}$$

$$= Ne^{-\frac{(E_{phot}-E_{res})^2}{2\sigma^2}} \tag{5.5.6}$$

$N = (\sigma\sqrt{2\pi})^{-1}$ is the normalizing constant of the Gaussian and σ its deviation. The general form of a Gaussian has been used instead of (5.5.2), since we demand that the full width at half maximum (FWHM) of the Gaussian equals the experimental line width Γ_{exp}:

$$\begin{aligned} \text{FWHM} &= 2\sigma\sqrt{2ln2} \stackrel{!}{=} \Gamma_{exp} \\ \Rightarrow \quad \sigma &= \frac{\Gamma_{exp}}{2\sqrt{2ln2}} \end{aligned} \tag{5.5.7}$$

Due to the fact that $L(E_{phot}; E_{res}, \Gamma^R_d)$ is energy-normalized, one simply has to replace this function in the derived expression of the total cross section (4.1.9) by

$$\begin{aligned} G(E_{phot}) &= \frac{1}{\sigma\sqrt{2\pi}}\, e^{-\frac{(E_{phot}-E_{di})^2}{2\sigma^2}} \\ &= \frac{2}{\Gamma_{exp}}\sqrt{\frac{ln2}{\pi}}\, e^{-\frac{4ln2(E_{phot}-E_{di})^2}{\Gamma^2_{exp}}}\,, \end{aligned} \tag{5.5.8}$$

where (5.5.7) has been made use of in the second line.
Therefore the total cross section including Doppler broadening is given by

$$\sigma^D_{i\to d}(E_{phot}) = 4\frac{\pi^3 c^2 \hbar^3}{E^2_{di}} A^{hfs}_{d\to i} \frac{1}{\Gamma_{exp}} \sqrt{\frac{ln2}{\pi}}\, e^{-\frac{4ln2(E_{phot}-E_{di})^2}{\Gamma^2_{exp}}}\,, \tag{5.5.9}$$

with the experimental line width Γ_{exp}. Γ_{exp} is related to a given experimental resolution[5] by

$$\Gamma_{exp} \approx \frac{\Delta E}{E} E_{di}\,. \tag{5.5.10}$$

Thus, for $\Delta E/E = 1/20000$ and with the typical value $E_{di} \approx 3.6\,\mathrm{eV}$, we get $\Gamma_{exp} = 1.8 \times 10^{-4}\,\mathrm{eV}$.

5.6 Spectra

In this section the main result of this work is presented: the optical spectra of the resonant fluorescence process for titaniumlike $^{209}Bi^{61+}$ ions. The absorption cross section as a function of energy and wavelength in *vacuum* with different experimental line widths Γ_{exp} and under external magnetic fields of 0 T, 1 T and 8 T is visualized.
The values from table 5.1 have been used, except for the energy levels of the fine structure E_{J_d}, E_{J_i}, where the fine structure energy splitting $E_{J_d} - E_{J_i} = E^{FS} = 3.604705\,\mathrm{eV}$ from [4] has been employed instead[6], which is judged accurate. This corresponds to a wavelength $\lambda^{FS} = 343.9510\,\mathrm{nm}$.

In figures 5.1, 5.2 $\sigma^D(E_{phot})$ and $\sigma^D(E_\lambda)$ are plotted with $B = 0\,\mathrm{T}$ and $\Gamma_{exp} = 1 \times 10^{-5}\,\mathrm{eV}$, so that only the hyperfine structure peaks are present. The corresponding numerical values of the peak positions, as well as the identity of the transitions are given in table 5.7.

[5] $E = \frac{hc}{\lambda}$.
[6] "Quad" value of $1/\lambda$, table 2, [4].

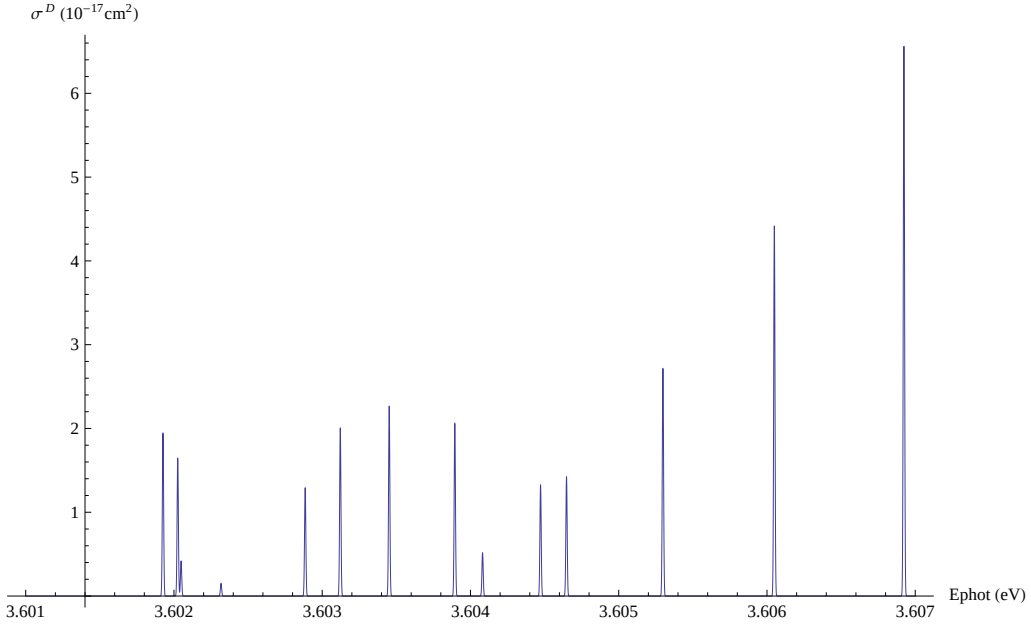

Figure 5.1: Hyperfine transition peaks for the case of a zero external magnetic field. Plotted is $\sigma^D(E_{phot})$, with $\Gamma_{exp} = 1 \times 10^{-5}$ eV. The fine-structure peak, i.e. the one for the hypothetical case of a vanishing nuclear spin lies at $E^{FS} = 3.604705$ eV.

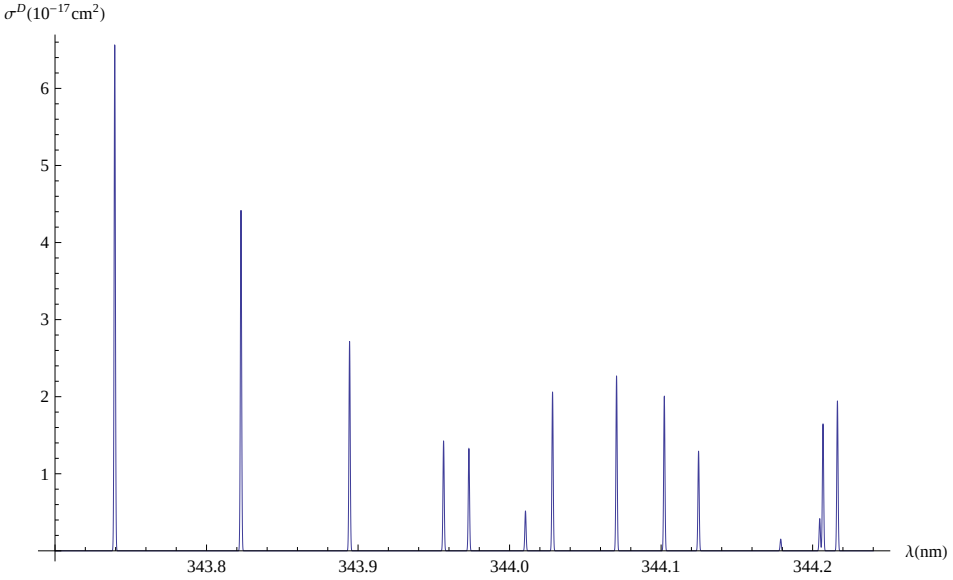

Figure 5.2: Hyperfine transition peaks; $\sigma^D(\lambda)$; $\Gamma_{exp} = 1 \times 10^{-5}$ eV.

Table 5.7: Hyperfine structure transitions, corresponding resonant wavelength and energy.

#	F_i	F_d	λ_{di}(nm)	$E_{di}(eV)$	#	F_i	F_d	λ_{di}(nm)	$E_{di}(eV)$
1	$\frac{13}{2}$	$\frac{15}{2}$	343.7394	3.606924	8	$\frac{9}{2}$	$\frac{9}{2}$	344.0706	3.603452
2	$\frac{11}{2}$	$\frac{13}{2}$	343.8227	3.606050	9	$\frac{7}{2}$	$\frac{7}{2}$	344.1021	3.603122
3	$\frac{9}{2}$	$\frac{11}{2}$	343.8944	3.605298	10	$\frac{5}{2}$	$\frac{5}{2}$	344.1247	3.602885
4	$\frac{7}{2}$	$\frac{9}{2}$	343.9564	3.604648	11	$\frac{13}{2}$	$\frac{11}{2}$	344.1790	3.602317
5	$\frac{13}{2}$	$\frac{13}{2}$	343.9732	3.604473	12	$\frac{11}{2}$	$\frac{9}{2}$	344.2047	3.602048
6	$\frac{5}{2}$	$\frac{7}{2}$	344.0105	3.604082	13	$\frac{5}{2}$	$\frac{3}{2}$	344.2069	3.602025
7	$\frac{11}{2}$	$\frac{11}{2}$	344.0284	3.603894	14	$\frac{9}{2}$	$\frac{7}{2}$	344.2164	3.601926
					15	$\frac{7}{2}$	$\frac{5}{2}$	344.2164	3.601926

Note that the difference of wavelengths among transitions 14 and 15 in table 5.7 is less than 0.5×10^5 nm, causing the corresponding peaks in Figure 5.2 to be indistinguishable at the set level of resolution. The small difference between peaks 13 and 14 is still visible, bringing the total count of visible transitions to 14 out of 15.

Still with $\Gamma_{exp} = 1 \times 10^{-5}$ eV but with $B = 1$ T, the spectra in figures 5.3 and 5.4 arise. There is now an interaction between the magnetic moments of the atom and the external field and the Zeeman splitting takes place. The resolution 36×10^4 is large enough to uncover many of the 410 Zeeman peaks out of the hyperfine ones. However the modulus of the Zeeman splitting correction to the resonance energy (peak position) $|\Delta E^{Zeem}_{M_{F_d}} - \Delta E^{Zeem}_{M_{F_i}}|$ is of the same magnitude as the line width or often less (compare with table 5.8), so that even the thinnest structures visible may be composed of overlapped peaks.

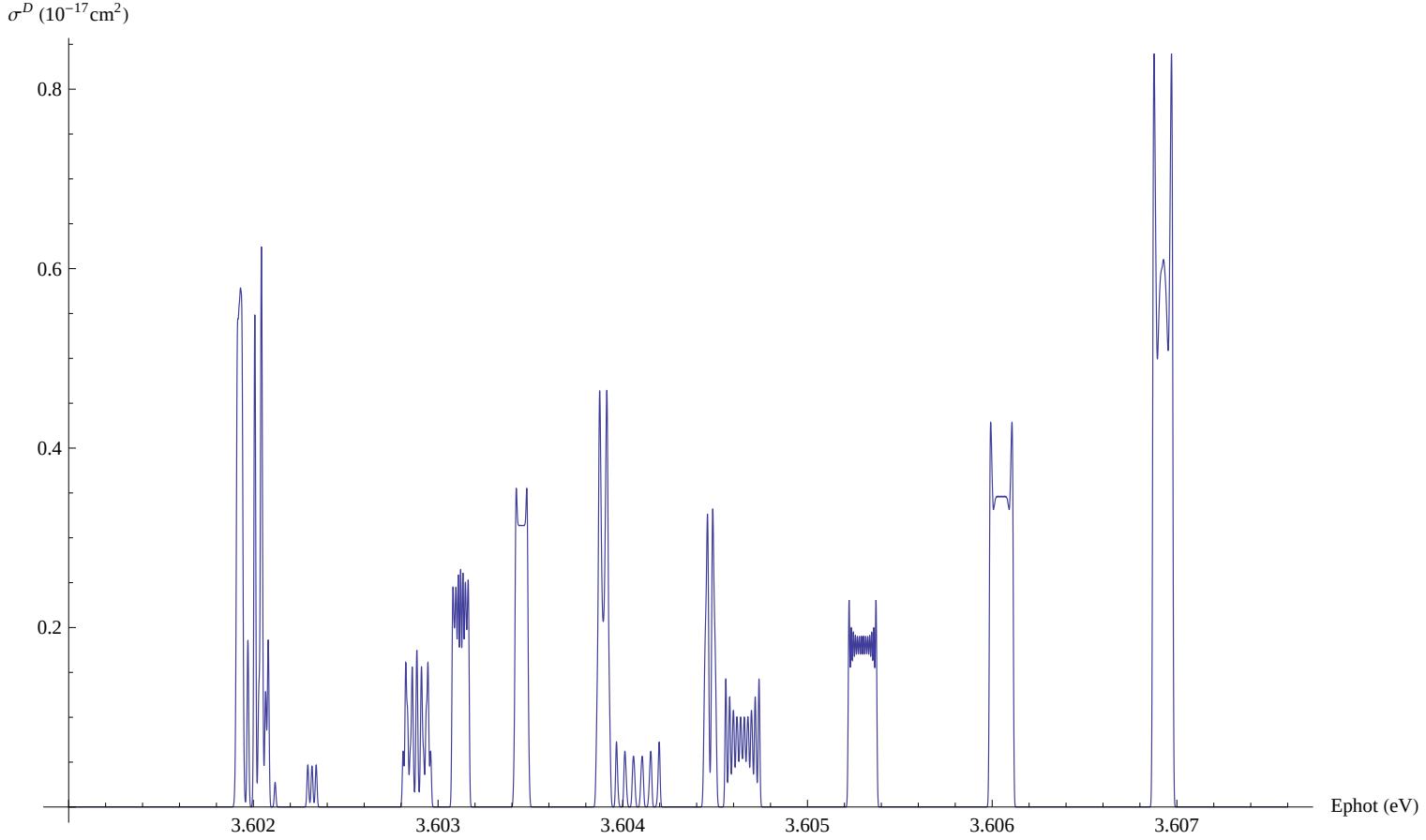

Figure 5.3: Doppler-broadened spectrum $\sigma^D(E_{phot})$ with with a resolution $\frac{\Delta E}{E} = 36 \times 10^4$ and an external magnetic field $B = 1T$. The fine structure resonance energy lies at $E^{FS} = 3.604705\,\mathrm{eV}$.

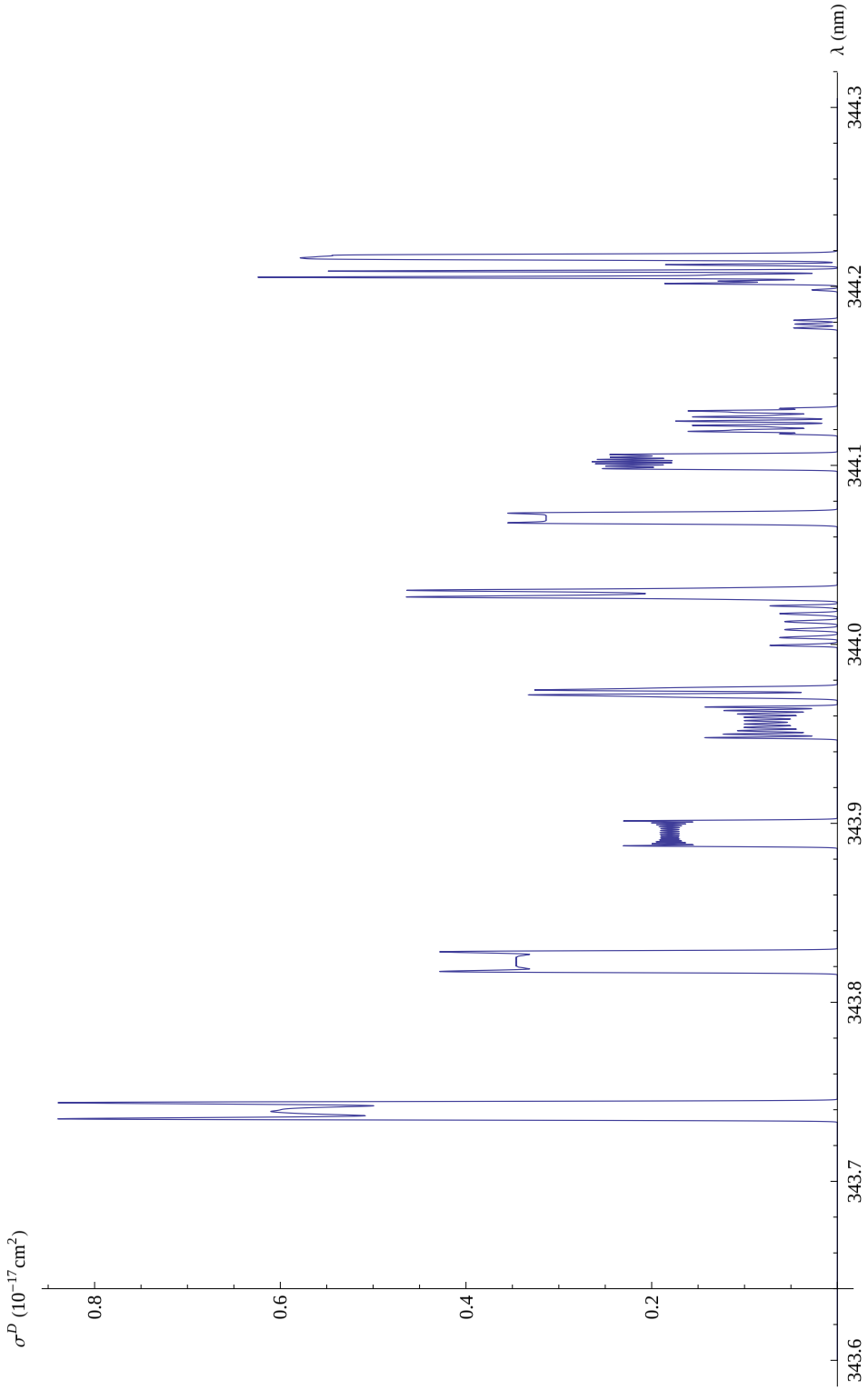

Figure 5.4: $\sigma^D(\lambda)$; $\frac{\Delta E}{E} = 36 \times 10^4$; $B = 1T$.

Decreasing the resolution to a realistic level, the Zeeman levels are present, but not resolvable. In Figure 5.5 a plot of (5.5.9) with $\Gamma_{exp} \equiv 1.8 \times 10^{-4}\,\mathrm{eV}$ and $B = 1\,\mathrm{T}$ can be seen.

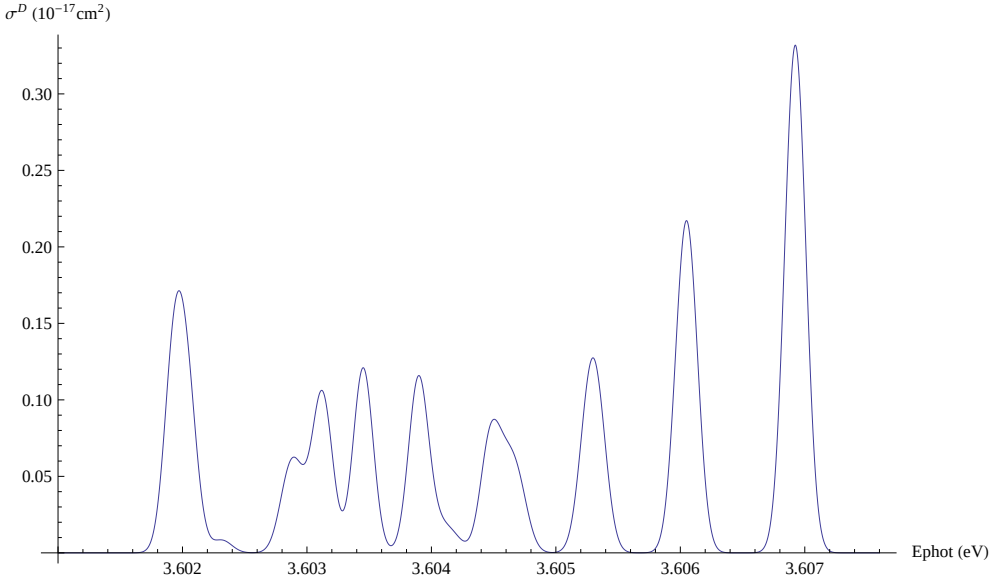

Figure 5.5: Doppler-broadened spectrum $\sigma^D(E_{phot})$ with a resolution $\frac{\Delta E}{E} = 2 \times 10^4$ and an external magnetic field $B = 1\,\mathrm{T}$.

In Figure 5.6 the same stands as a function of wavelength with the positions of the fine structure peaks marked with red lines.

We perform a small test for the peak heights: the Doppler broadening decreases the peak maximum values via the convolution as [5]

$$\sigma^D_{i\to d}(E_{phot}) \approx \sqrt{\pi ln 2}\,\frac{\Gamma^R_d}{\Gamma_{exp}}\sigma_{i\to d}(E_{phot})\,. \tag{5.6.1}$$

In our case, the value of the natural-width cross section at resonance ($E_{di} \approx 3.6\,\mathrm{eV}$) is[7]:

$$\sigma_{i\to d}(E_{di}) = 2\frac{\pi c^2\hbar^2}{E^2_{di}}\frac{(2J_d+1)A^{hfs}_{d\to i}}{A^{FS}_{d\to f}} \approx 1.9 \times 10^{-10}\,\mathrm{cm}^2\,, \tag{5.6.2}$$

so that we expect:

$$\sigma^D_{i\to d}(E_{di}) \approx 1.5\,\frac{1 \times 10^{-12}\,\mathrm{eV}}{1.8 \times 10^{-4}\,\mathrm{eV}} 1.9 \times 10^{-10}\,\mathrm{cm}^2 \approx 1.6 \times 10^{-18}\,\mathrm{m}^2\,. \tag{5.6.3}$$

This indeed corresponds to the order-of-magnitude in the above figures.

[7]The resonance value of a Lorentzian $L(E_{res};\Gamma) = \frac{2}{\Gamma\pi}$.

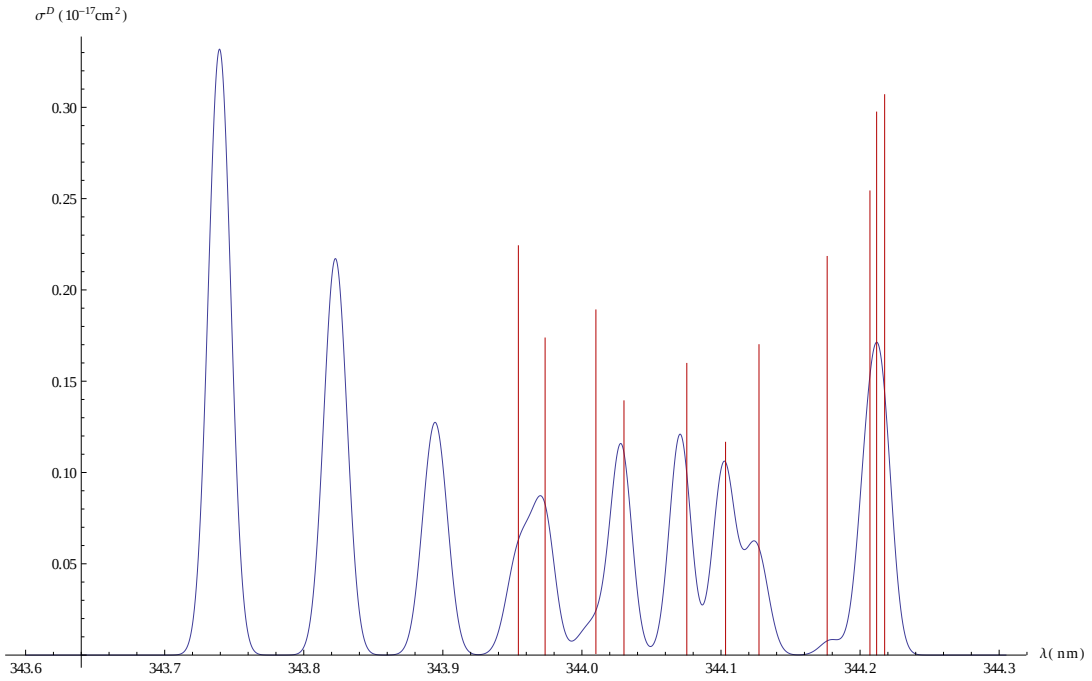

Figure 5.6: Doppler-broadened spectrum $\sigma^D(\lambda)$; resolution $\frac{\Delta\lambda}{\lambda} = 2 \times 10^4$, external magnetic field $B = 1\,\mathrm{T}$. The lines drawn in the figure indicate the hyperfine structure peaks, which are displayed separately in figures 5.1, 5.2. The corresponding exact numerical values can be extracted from table 5.7.

Table 5.8: Numerical values of properties of selected transitions. The numbering is based on the total 410 transitions. hW_J are the hyperfine energy splittings and $R_{i/d} = hW_{J_{i/d}}/\Delta E^{Zeem}_{M_{F_{i/d}}}$ the ratios of the hyperfine and Zeeman splitting energies of each level.

#	F_i	F_d	M_{F_i}	M_{F_d}	$A^{hfs}_{d\to i}$ (Hz)	E_{di} (eV)	hW_{J_i} (meV)	$\Delta E^{Zeem}_{M_{F_i}}$ (10^{-5}eV)	hW_{J_d} (meV)	$\Delta E^{Zeem}_{M_{F_d}}$ (10^{-5}eV)	R_i	R_d
16	$\frac{7}{2}$	$\frac{5}{2}$	$\frac{1}{2}$	$\frac{1}{2}$	7.29	3.60192	-1.93	-0.32	-4.71	-0.71	603.125	663.38
20	$\frac{9}{2}$	$\frac{7}{2}$	$\frac{1}{2}$	$\frac{1}{2}$	3.71	3.60192	-0.73	0.41	-3.51	0.29	-178.049	-1210.34
49	$\frac{11}{2}$	$\frac{9}{2}$	$\frac{11}{2}$	$\frac{9}{2}$	3.03	3.60203	0.67	8.76	-1.99	6.76	7.6484	-29.4379
108	$\frac{13}{2}$	$\frac{11}{2}$	$-\frac{11}{2}$	$-\frac{11}{2}$	0.14	3.60232	2.25	-11.34	-0.14	-10.96	-19.8413	1.27737
130	$\frac{5}{2}$	$\frac{5}{2}$	$\frac{1}{2}$	$\frac{1}{2}$	0.53	3.6029	-2.89	-1.91	-4.71	-0.71	151.309	663.38
146	$\frac{7}{2}$	$\frac{7}{2}$	$-\frac{1}{2}$	$-\frac{1}{2}$	0.35	3.60312	-1.93	0.32	-3.51	-0.29	-603.125	1210.34
177	$\frac{9}{2}$	$\frac{9}{2}$	$\frac{3}{2}$	$\frac{3}{2}$	1.79	3.60346	-0.73	1.22	-1.99	2.25	-59.8361	-88.4444
191	$\frac{11}{2}$	$\frac{11}{2}$	$-\frac{11}{2}$	$-\frac{11}{2}$	12.63	3.60387	0.67	-8.76	-0.14	-10.96	-7.6484	1.27737
205	$\frac{11}{2}$	$\frac{11}{2}$	$\frac{11}{2}$	$\frac{9}{2}$	2.3	3.6039	0.67	8.76	-0.14	8.96	7.6484	-1.5625
230	$\frac{5}{2}$	$\frac{7}{2}$	$\frac{1}{2}$	$-\frac{1}{2}$	1.6	3.6041	-2.89	-1.91	-3.51	-0.29	151.309	1210.34
274	$\frac{13}{2}$	$\frac{13}{2}$	$\frac{3}{2}$	$\frac{5}{2}$	3.81	3.6045	2.25	3.09	2.01	5.72	72.8155	35.1399
287	$\frac{7}{2}$	$\frac{9}{2}$	$-\frac{1}{2}$	$-\frac{3}{2}$	5.16	3.60462	-1.93	0.32	-1.99	-2.25	-603.125	88.4444
315	$\frac{9}{2}$	$\frac{11}{2}$	-$\frac{5}{2}$	-$\frac{3}{2}$	2.15	3.60529	-0.73	-2.03	-0.14	-2.99	35.9606	4.68227
336	$\frac{11}{2}$	$\frac{13}{2}$	$-\frac{5}{2}$	$-\frac{7}{2}$	15.86	3.60601	0.67	-3.98	2.01	-8.00	-16.8342	-25.125
371	$\frac{13}{2}$	$\frac{15}{2}$	$-\frac{9}{2}$	$-\frac{11}{2}$	26.55	3.60688	2.25	-9.28	4.46	-13.62	-24.2457	-32.746

In Figure 5.7 a plot with $\Gamma_{exp} \equiv 1.8 \times 10^{-4}\,\mathrm{eV}$ and $B = 8\,\mathrm{T}$ (typical EBIT value) can be seen.

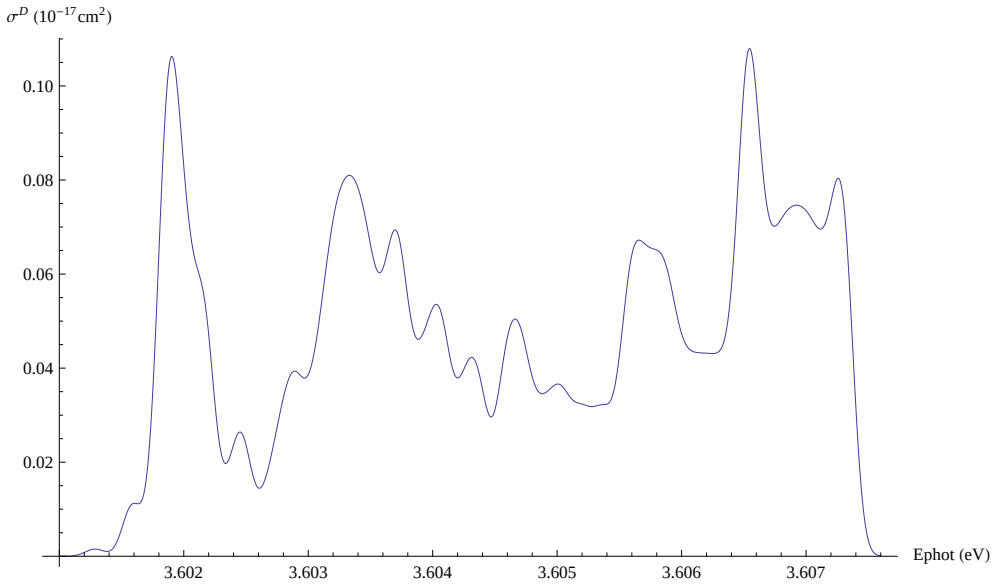

Figure 5.7: Doppler-broadened spectrum $\sigma^D(E_{phot})$; resolution $\frac{\Delta E}{E} = 2 \times 10^4$, external magnetic field $B = 8T$.

An interesting result is obtained from the decrease of the experimental width down to $\Gamma_{exp} = 1 \times 10^{-5}\,\mathrm{eV}$ in Figure 5.8. Here the large increase of the Zeeman splitting energies due to the magnetic field and thus the decrease of the ratio between hyperfine structure and Zeeman splitting energies is visualized by the dense arrangement of the peaks, which fill the whole energy range.
The maximum and minimum values among the 410 transitions of the ratios between the hyperfine and Zeeman splitting energies $R_{i/d} = hW_{J_{i/d}}/\Delta E^{Zeem}_{M_{F_{i/d}}}$ for the lower and upper level, respectively, are given in table 5.9.

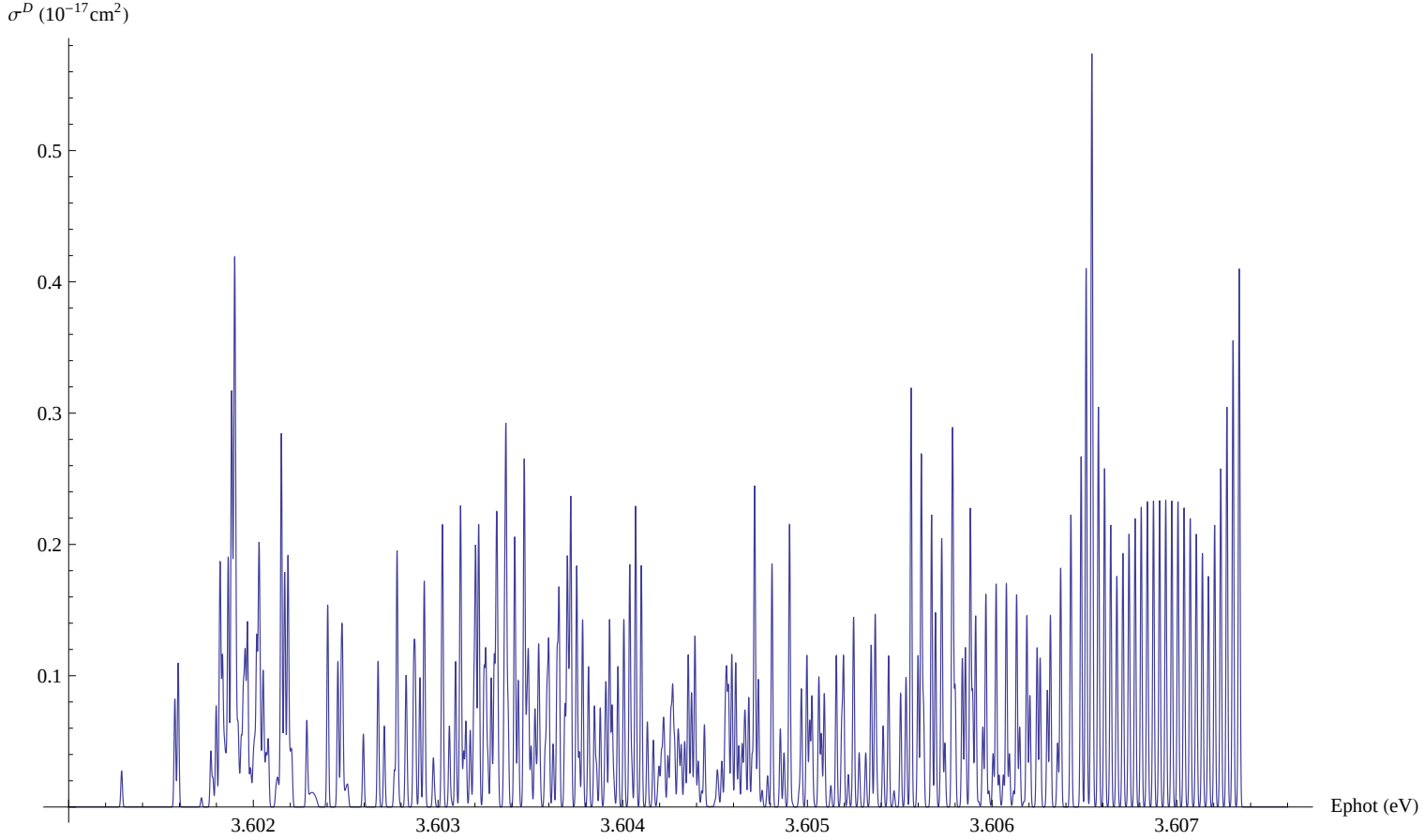

Figure 5.8: Doppler-broadened spectrum $\sigma^D(E_{phot})$ with a resolution $\frac{\Delta E}{E} = 3.6 \times 10^5$ and an external magnetic field $B = 8\,\mathrm{T}$.

Table 5.9: Extreme values of the ratios $R_{i/d} = hW_{J_{i/d}}/\Delta E^{Zeem}_{M_{F_{i/d}}}$ of the hyperfine and Zeeman splitting energies for a 1-Tesla and an 8-Tesla external magnetic field.

B(T)	R_i^{min}	R_i^{max}	R_d^{min}	R_d^{max}
1	7.6	603.1	1.3	1210.3
8	1.0	75.6	0.2	148.9

For 8 T the Zeeman splitting can be larger that the hyperfine. This is not the exception of some values: 310 out of 410 transitions give a ratio R_i or R_d less than 10, our tolerance limit. This means that for a 8 T magnetic field the first-order perturbation approach in the calculation of the Zeeman splitting is not appropriate; the strong-field limit of the Zeeman effect (*Paschen-Back effect*) has been reached. Same holds for 6 T, where 292 transitions fail the test.
For $B = 1$ T 100 of 410 transitions exist, where one of the ratios R_i, R_d is less than 10. This case deserves a more thorough examination. It has been observed that these peaks with low ratio are the ones around the positions given in table 5.10 (compare with figure 5.3). As one can see, they belong to

Table 5.10: Low-ratio peak neighborhoods with corresponding F quantum numbers for $B = 1$ T to be compared with figure 5.3 and table 5.8.

#	example from table 5.8	hfs transition	E_{phot} (eV)
1	49	$\frac{9}{2} \to \frac{11}{2}$	3.6020
2	108	$\frac{11}{2} \to \frac{13}{2}$	3.6023
3	205	$\frac{11}{2} \to \frac{11}{2}$	3.6039
4	315	$\frac{11}{2} \to \frac{9}{2}$	3.6053
5	336	$\frac{13}{2} \to \frac{11}{2}$	3.6061

higher hyperfine transitions. Opposed to them, the rest of the peak groups correspond to transitions between F-values of $\frac{9}{2}$, $\frac{7}{2}$, $\frac{5}{2}$. This explains why the former ones present low hyperfine/Zeeman splitting energy ratios: in the upper hyperfine levels the electrons interact less strong with the multipole

moments of the nucleus than in the lower ones, letting thus the interaction energy due to the external magnetic field, e.g. the Zeeman splitting, dominate. An exception to this tendency is the region of 3.607 eV, which is characterized by high ratios. The relatively high hyperfine interaction energy (distance from E^{FS}) counteracts the above mentioned effect and keeps the ratio high.
For $B = 1\,\mathrm{T}$ the perturbation theory ansatz applies to some specific energy regions. Since the peak groups in figure 5.3 are clearly separated from each other, as opposed to the 8 T case, a comparison with the experiment can be achieved so long as the resolution is high enough to keep the low-ratio peaks apart from the high-ratio ones. Such a spectrum is the one in Figure 5.5 for example.

Chapter 6

Summary and Outlook

Calculating level energies in highly charged ions keeps representing a great theoretical challenge. First of all, a many-body problem has to be solved in order to obtain the interaction energies between electrons. Secondly, the presence of a nuclear field implies the consideration of the Coulomb interaction between electrons and the nucleus. In the case when the nucleus has a magnetic dipole or electric quadrupole moment, there is an additional interaction between the nuclear and electronic multipole moments. This then gives rise to the hyperfine splitting of the atomic levels, which in the presence of a static external magnetic field leads additionally to the Zeeman effect. Once the external field becomes strong enough, one enters the Paschen-Back regime, where crossings of the energy levels are expected.

In the present work, we address these issues in titaniumlike bismuth, motivated by its high nuclear spin and thus its Zeeman splitting energy corresponding to the visible region of the spectrum. The calculations have been carried out in the boundaries between the weak and strong external magnetic field.

First the hyperfine spectrum at $B = 0\,\mathrm{T}$ has been obtained successfully with the help of multiconfiguration Dirac-Fock calculation using the General Relativistic Atomic Structure Package (GRASP) package of codes. After having calculated the corresponding spectra, we conclude that almost all transition peaks can be clearly distinguished with the choice of a very small experimental width. This has served as a first validation of the computational model. Concerning the Zeeman splitting, it has been concluded that for a 1-Tesla strength of the external magnetic field, the calculation of the Zeeman interaction in first-order perturbation theory is a valid approximation for most peaks. In the other domains allowed transitions between $3d^4$ levels with $J = 2, 3$ exhibit a hyperfine/Zeeman splitting ratio less than the tolerance

value 10, considered as the threshold for the applicability of perturbation theory. For a 8-Tesla field, more than half of the transitions fail this. For the present, the interest lies in the experimental confirmation of this fact through a comparison of theoretical and measured spectra.

During an actual EBIT experiment, the magnetic field is indeed 8 T, thus it is in the order where perturbation theory ceases to apply. However, this holds true only for the case when electrons from relatively outer shells are involved, such as in titaniumlike bismuth. In the hydrogenlike case the, hyperfine structure splitting would be large enough to ensure a high ratio, but would shift the spectrum beyond the high energy end of the visible part.

Concerning the numerical calculations with the GRASP programs, various parameters have been investigated concerning their influence on the fine-structure transition rate and level energies and hence the optimal settings have been chosen. These calculations were necessary in order to obtain good atomic state functions. These were then used in the programs "hfs92" and "gfactor2001" in order to compute the hyperfine interaction constants and the g_J factor of the fine structure splitting. Thus, the determination of the hyperfine and Zeeman splitting energies was carried out. This was another innovation in this work.

Using a projection operator formalism on the continuum- and bound states involved in the resonant fluorescence process, an expression for the cross section of the interaction between the atom and the electromagnetic field, for example, a weak laser field, has been derived, leading thus to the calculation of the absorption spectra that have been discussed previously.

Considerable insight in the behavior of the spectra with respect to the Doppler broadening and the influence of the magnetic field has been gained, opening the way towards future, even more detailed calculations. The next step in the theoretical calculation would be to conduct a non-degenerate perturbation theory approach to the interaction of the magnetic moments in the atom with the external field. To this end, non-diagonal matrix elements of both magnetic operators need to be evaluated with the existing atomic wave functions. This could lead eventually to the insight, that for high magnetic fields, the Zeeman splitting energy, after overcoming a nonlinear (e.g. quadratic) zone, is again linear in B, after regions with crossings. Certainly, further extensions may be undertaken in the theory. One suggestion would address QED corrections to the hyperfine splitting to be calculated, however, given the large number of electrons, to perform such calculations would be a great undertaking.

From the experimental point of view, two-photon laser spectroscopy and

saturated absorption spectroscopy are methods that could help increase the spectral resolution. Having both fine- and hyperfine structure splitting in the optical range, high-resolution spectroscopy could provide the accuracy needed for determining the nuclear magnetic moment. This would lead to further knowledge about nuclear electromagnetic properties.

Note that the Bohr-Weisskopf effect caused by the finiteness of the nuclear magnetization distribution has not been taken into account in our calculations, since no reliable information related to nuclear structure is available so far. However, a comparative calculation between a pointlike and a finite-size nucleus for bismuth can be carried out, in order to determine the influence on the energy levels of the $3d$ states, but this is not expected to be of great significance, due to the relatively large distance of these orbitals from the nucleus.

The dependence of the cross section on the emission angle and polarization of the fluorescence photons may be considered in further studies. This will be necessary when one wanted to compare the theoretical and experimental cross sections on an absolute scale, since in an actual experiment one can only detect photons under one or a few fixed solid angles. In addition, in case the isolated resonances approximation assumed in the derivation of the cross section is not adopted, the interference among the decay channels of each state is to be included.

The calculations may be extended relatively easily to further elements in future, leading thus to conclusions about evolutions of the effects. By comparing spectra among isotopes, which are expected to exhibit completely different profiles (since e.g. some of them do not possess a nuclear spin), one could use such absorption or fluorescence spectra to measure the isotopic abundance in, for example, astronomical objects.

In tokamak plasmas, high confining magnetic fields dominate and a large variety of ions is present. Again, from the investigation of the visible spectrum not only identification of these elements in the plasma, but also characterization of their excitation state could be achieved. Furthermore, their temperature may be determined based on the line broadening. In order to perform all these analytical examinations, a good theoretical description, followed by accurate numerical predictions, have to be available. It is within this concept that this bachelor thesis has been carried out, applying rigor and considering details in a controlled manner throughout the derivations and calculations.

Appendix

A General Relativistic Atomic Structure Package

In this chapter the functionalities of the General-purpose Relativistic Atomic Structure Package (GRASP), an implementation of the multiconfiguration Dirac-Fock method, are presented. The information and technical details as described in the papers [2, 9, 10, 13, 19] are summarized.

A.1 Overview of the Package

GRASP is a suite of programs written in FORTRAN for multiconfigurational relativistic atomic structure calculations with large configuration state function (CSF) lists. In the present work, we employed its version GRASP92 [19], with some auxiliary programs written as an extension of the original package [10, 13]. Using a fully relativistic approach, theoretical data describing atomic spectra, e.g. energy levels and radiative decay rates, can be calculated. A typical calculational session thereby includes the following general steps:

(a) definition of nuclear data,

(b) generation and manipulation of configuration state lists,

(c) generation of angular coefficients needed for the calculation of matrix elements with multiconfiguration wave functions,

(d) initial estimates for radial functions,

(e) application of the self-consistent field procedure for obtaining radial functions and configuration expansion coefficients,

(f) relativistic configuration interaction calculations to include other operators in the Hamiltonian,

(g) evaluation of atomic properties like transition probabilities, hyperfine interaction constants and g factors.

A.2 Description of the Individual Programs

geniso

After the input of the nuclear data, that is, atomic number, mass number, nuclear spin quantum number, dipole and quadrupole moment, a nuclear

data file .iso is created, which is to be used by the subsequent programs of the package. The nucleus can be treated either as a point charge or its extended charge distribution may be described by the two-parameter Fermi distribution given by equation (2.6.2).

gencsl

Here, a list of jj-coupled configuration state functions are generated (configuration symmetry list). This is done by considering electronic excitations with respect to one or more reference states ("*reference* peel subshell configurations"; in our case only $3d^4$) towards an active set of orbitals belonging to the peel subshells in general.

Taking correlation of the orbitals into account, *gencsl* generates all possible CSFs that include, for example, single substitutions between the peel subshells: the occupation of one of the subshells belonging to the reference subshell configuration[1] defined by the user is reduced by 1 and the occupation for any other subshell in the same configuration increased by 1. Additionally, *correlation functions* can be defined by the user, which are also taken into account in the substitutions and hence in the construction of the ASFs.

All replacements are consistent with the limits of subshell occupation and applied in such a way that the total atomic angular momentum and parity keep the same value as those of the reference CSFs. For example, let us assume that the user has defined the reference subshell configuration to be $3s^0\ 3p^6\ 3d^6$. A possible single replacement could be $3s^1\ 3p^6\ 3d^5$ or, if for example all $n = 4$ subshells are defined as additional correlation functions, $3s^0\ 3p^6\ 3d^5\ 4s^1$.

Multiple substitutions are also possible. Note that in contrast to the peel subshells, a list of *core subshells* can be defined during the input, from or towards which no electronic replacements take place. In the example above that would be $1s^2\ 2s^2$.

In principle, the larger the configuration symmetry list, the more accurate will the calculation be. However, the number of the CSFs grows fast, especially with multiple substitutions allowed: in our case of the titaniumlike ground-state configuration, allowing orbitals up to $n = 3$ and considering only configurations with $J = 2, 3$ without substitutions corresponds to 14 CSFs, whereas allowing single and double substitutions only within the $n = 3$

[1] This is often referred to as the "spectroscopic" configuration.

shell leads to 243 CSFs; allowing peel orbitals of the $n = 3, 4$ shells to be substituted, the procedure leads to ≈ 65.000 CSFs. The size of the configuration symmetry list is decisive for the convergence of the calculation.

erwf

This program performs an initial estimate of the radial wave functions $P_{n\kappa}(r)$ and $Q_{n\kappa}(r)$ of the Dirac orbitals. These estimates can be obtained by solving the Dirac equation in the Thomas-Fermi potential, as screened hydrogenic functions, or by using radial files of previous calculations that are trustworthy. By the latter method, good starting wave functions are provided for the self-consistency procedure, which eventually helps overcoming convergence problems or simply reduces the number of iterations needed. Nevertheless, the final results are independent of the choice of initial estimate wave functions.

GRASP makes use of a radial grid in order to tabulate the values of the subshell radial wave functions. These are thus considered vanishing beyond their maximum tabulation point (MTP) on the radial grid. The value of the MTP is given in a summary (.sum) file along with the coefficients and exponents describing the asymptotic behavior of the wave functions.

genmcp

The angular coefficients 2.2.7 are calculated by algebraically performing spin-angular integrations for the matrix elements of the many-electron Dirac-Coulomb Hamiltonian.

rscf

For a given list of CSFs, the radial wave functions are optimized and the eigenvalue problem for the mixing coefficients c_{s_Γ} is solved simultaneously according to the self-consistency procedure described in Section 2.5.1. One may choose between an Optimized Level (OL) or an Average Level (AL) procedure [2]. The result is a new set of radial wave functions together with mixing coefficient values, which together define the atomic state function (ASF).

rci

The relevant informations for this package have been already given in Section 5.4.

oscl

This program calculates the radiative decay rate $A^{FS}_{d\to i}$ between the fine structure levels by usage of a radial wave function set originating from an rscf calculation, and configuration mixing coefficients from an rscf or rci run. Other related transition parameters for multipole transitions like the Einstein B coefficients [7], oscillator strengths, total radiative widths and lifetimes are also provided.

hfs92

This program calculates the hyperfine interaction constants A_J, B_J introduced in Section 4.2. It makes use of the nuclear data in the .iso file generated by geniso, the configuration symmetry list from gencsl, the radial wave function file and the corresponding mixing coefficients file.

gfactor2001

This program evaluates g_J factors of fine structure levels and subsequently the leading QED correction due to the interaction of the free electron with the quantized vacuum is added to this value. It needs the same inputs as rhfs, except for the .iso file.

B Projection Operators

B.1

In this appendix we evaluate the the operator $R\Phi(z)R$ – appearing in the derivation of the resonance fluorescence cross section – in the lowest-order approximation. Starting from the definition of $\Phi(z)$,

$$[R(z - H_0 - V)R]\Phi(z) = R\,,$$

and taking into account that R and H_0 commute and as well that $R^2 = R$, we write

$$\begin{aligned}(z - H_0)R\Phi(z)R &= R + RVR\Phi(z)R \\ (z - H_0)R^2\Phi(z)R &\approx R \\ R(z - H_0)R^2\Phi(z)R &\approx R \\ R\Phi(z)R &\approx R[R(z - H_0)R]^{-1}. \end{aligned} \tag{B.1}$$

B.2

Here we give in detail the calculation of another intermediate step in Section 3.3. Here we can use the result of the previous Appendix (B.1):

$$\begin{aligned}&\langle Q\Phi_d|Q[z - H - VR\Phi(z)RV]|Q\Phi_d\rangle \\ &\approx \langle Q\Phi_d|Q[z - H_0 - V - V\underbrace{R[R(z - H_0)R]^{-1}}_{RG_0^R(z)R}V]Q|Q\Phi_d\rangle \\ &= \langle Q\Phi_d|Q[z - H_0 - V]Q|Q\Phi_d\rangle - \langle Q\Phi_d|QVRG_0^R(z)RVQ|Q\Phi_d\rangle \\ &= \langle Q\Phi_d|z - H_0 - V|Q\Phi_d\rangle - \underbrace{\langle Q\Phi_d|VRG_0^R(z)RV|Q\Phi_d\rangle}_{\alpha} \\ &= z\underbrace{\langle Q\Phi_d|Q\Phi_d\rangle}_{1} - \underbrace{\langle Q\Phi_d|H_0|Q\Phi_d\rangle}_{E_d} - \underbrace{\langle Q\Phi_d|V|Q\Phi_d\rangle}_{0} - \alpha \\ &= (z - E_d) - \langle Q\Phi_d|VRG_0^R(z)RV|Q\Phi_d\rangle \end{aligned} \tag{B.2}$$

showing thus (3.3.18). In (B.2), use has been made of the property $Q^2 = Q$ of the projection operator. The penultimate term in (B.2) is equal to zero because the interaction operator V describes transitions between different subspaces only and has diagonal elements equal to zero as mentioned in Section 3.2.

C $3j-$ and $6j-$ Symbols

In order to evaluate $\sum_f A_{d\to f}^{hfs}$, we need to assess the sum

$$\sum_{F_f, M_{F_f}} (2F_d + 1)(2F_f + 1) \begin{pmatrix} F_f & 1 & F_d \\ -M_{F_f} & M_{F_f} - M_{F_d} & M_{F_d} \end{pmatrix}^2 \begin{Bmatrix} J_f & F_f & I \\ F_d & J_d & 1 \end{Bmatrix}^2, \tag{C.1}$$

since $A^{FS}_{d\to f}$ in (4.1.4) depends only on J. Here, J_{phot}=1, as mentioned in Chapter 4.1. For given values of F_d and M_{F_d}:

$$\begin{aligned}
&\sum_{M_{F_f}} \begin{pmatrix} F_f & 1 & F_d \\ -M_{F_f} & M_{F_f}-M_{F_d} & M_{F_d} \end{pmatrix}^2 \\
&= \begin{pmatrix} F_f & 1 & F_d \\ -M_{F_d}+1 & -1 & M_{F_d} \end{pmatrix}^2 + \begin{pmatrix} F_f & 1 & F_d \\ -M_{F_d}-1 & 1 & M_{F_d} \end{pmatrix}^2 \\
&+ \begin{pmatrix} F_f & 1 & F_d \\ -M_{F_d} & 0 & M_{F_d} \end{pmatrix}^2
\end{aligned} \tag{C.2}$$

because the $3j-$symbol remains nonzero only for 3 values of M_{F_f}:

$$M_{F_d}-1 \le M_{F_f} \le M_{F_d}+1 \tag{C.3}$$

Using analytical expressions[2] for the $3j-$symbol, one can show that

$$\sum_{M_{F_f}} \begin{pmatrix} F_f & 1 & F_d \\ -M_{F_f} & M_{F_f}-M_{F_d} & M_{F_d} \end{pmatrix}^2 = \frac{1}{2F_d+1}\,. \tag{C.4}$$

Thus (C.1) becomes

$$\sum_{F_f}(2F_f+1) \begin{Bmatrix} J_f & F_f & I \\ F_d & J_d & 1 \end{Bmatrix}^2 . \tag{C.5}$$

We use the properties of the $6j$-symbol[3]:

$$\begin{Bmatrix} J_f & F_f & I \\ F_d & J_d & 1 \end{Bmatrix}^2 = \begin{Bmatrix} J_f & I & F_f \\ F_d & 1 & J_d \end{Bmatrix}^2 = \begin{Bmatrix} J_f & I & F_f \\ F_d & 1 & J_d \end{Bmatrix} \begin{Bmatrix} F_d & 1 & F_f \\ J_f & I & J_d \end{Bmatrix} \tag{C.6}$$

which yields[4]

$$\sum_{F_f}(2F_f+1) \begin{Bmatrix} J_f & F_f & I \\ F_d & J_d & 1 \end{Bmatrix}^2 = \frac{1}{2J_d+1}\,. \tag{C.7}$$

[2]See [14], p. 437, 438 .
[3]See [17], p.1063, 1064 .
[4]We make use of the orthogonality relation (C.35c) in [17], p.1065 .

Bibliography

[1] D. Budker, D. F. Kimball, and D. P. DeMille. *Atomic Physics*. Oxford university press, second edition, 2008.

[2] K. G. Dyall, I. P. Grant, C. T. Johnson, F. A. Parpia, and E. P. Plummer. Grasp: A general-purpose relativistic atomic structure program. *Comput. Phys. Commun.*, 55:425–456, 1989.

[3] Herman Feshbach. A unified theory of nuclear reactions ii. *Annals of Physics*, 19:287–313, 1962.

[4] C. Froese Fischer and S. Fritzsche. Magnetic-dipole transitions between the lowest $3d^4$ $J = 2 - 3$ transitions in highly charged titanium-like ions. *Journal of Physics B: Atomic, Molecular and Optical Physics*, 34(24):L767, 2001.

[5] C. J. Foot. *Atomic Physics*. Oxford Master Series In Physics. Oxford University Press, 2006.

[6] J. D. Gillaspy. Highly charged ions. *J. Phys. B: At. Mol. Opt. Phys.*, 34:R93–R130, 2001.

[7] I. P. Grant. Gauge invariance and relativistic radiative transitions. *J. Phys. B: At. Mol. Opt. Phys.*, 7:1458, 1974.

[8] S. L. Haan and V. L. Jacobs. Projection-operator approach to the unified treatment of radiative and dielectronic recombination. *Phys. Rev. A*, 40:80, 1989.

[9] P. Jönsson, X. He, C. Froese Fischer, and I.P. Grant. The grasp2k relativistic atomic structure package. *Comput. Phys. Commun.*, 177:597–622, 2007.

[10] P. Jönsson, F. A. Parpia, and C. Froese Fischer. HFS92: A program for relativistic atomic hyperfine structure calculations. *Computer Physics Communications*, 96:301–310, 1996.

[11] W. R. Johnson and G. Soff. The Lamb shift in Hydrogen-like atoms. *At. Data Nucl. Data Tables*, 33:405, 1985.

[12] Walter R. Johnson. *Atomic Structure Theory.* Springer, 2007.

[13] T. Kondo. Gfactor2001:a program for relativistic atomic g-factor calculations. *Computer Physics Communications*, (146):261–270, 2002.

[14] L. D. Landau and E. M. Lifshitz. *Quantum Mechanics (Non-relativistic theory)*, volume 3. Butterworth-Heinemann, third edition, 1977.

[15] J. R. Crespo López-Urrutia. The visible spectrum of highly charged ions: A window to fundamental physics. *Canadian Journal of Physics*, 86:111–123, 2008.

[16] J. B. Mann and W. R. Johnson. Breit interaction in multielectron atoms. *Phys. Rev. A*, 4:41, 1971.

[17] Albert Messiah. *Quantum Mechanics*, volume 2. North-Holland Publishing Company Amsterdam-Oxford, 1975.

[18] P. J. Mohr. Self-energy correction to one-electron energy levels in a strong Coulomb field. *Phys. Rev. A*, 46:4421–4424, 1992.

[19] F. A. Parpia, C. Froese Fischer, and I. P. Grant. Grasp92: A package for large-scale relativistic atomic structure calculations. *Comput. Phys. Commun.*, 94:249, 1996.

[20] Roxana Schiopu. Effect on the nuclear charge distribution on dielectronic resonances for heavy few-electrons ions. Master's thesis, University of Bucarest, June 2004.

[21] V. M. Shabaev. Hyperfine structure of hydrogen-like ions. *J. Phys. B: At. Mol. Opt. Phys.*, 27:5825–5832, 1994.

[22] J. R. Taylor. *Scattering Theory.* Wiley, New York, 1972.

[23] S. A. Zapryagaev. *Optical Spectroscopy*, (47):9, 1979.

Acknowledgements

I wish first of all to thank Prof. Dr. Keitel and Dr. José Crespo for supervising this thesis.
I am especially grateful to Dr. Crespo for giving me the opportunity in February 2010 to carry out an internship in his EBIT group at the Max Planck Institute for Nuclear Physics, thus initiating me to the physics of ions and for introducing me later on to Dr. Zoltán Harman, with whom I have collaborated in the present work.
Zoltán has been an extremely patient and ever caring mentor and collaborator, who welcomed me in his theory group from the beginning and supported me until the very end of my work. During our work together he took considerable amount from his precious time for discussions and helpful advice. Thanks to him I acquired deep insight in atomic physics. For all these I offer him my warmest gratitude.
Dr. Zoltán Harman, Prof. Yousef Salamin, Dr. Jacek Zatorski, Benjamin Galow, all other group members, as well as Veerle Sterken, ensured with their company a most pleasant time at the Institute.
Thanks to Dr. Jacek, Benjamin, Veerle and of course Zoltán for pointing out typographical errors in the final version of the thesis.
Finally special thanks to my family and friends, both in Greece and in Germany, who have been standing next to me during my entire study period giving me much strength and hope at all occasions.

Erklärung

Ich versichere, dass ich diese Arbeit selbstständig verfasst und keine anderen als die angegebenen Quellen und Hilfsmittel benutzt habe.

Heidelberg, den 13. Juli 2011,